SINGLE DROPLET DRYING AT HIGH TEMPERATURES

Andrew Bayly
PhD students: Wael Ebrahim, Tien Nguyen
School of Chemical and Process Engineering, University of Leeds, U.K.
IFPRI International Fine Particle Research Institute
UNIVERSITY OF LEEDS

1 Key Developments

Filament rig
- Rig and technique development
- Detailed analysis of HPMC, Sucrose, Sodium Silicate
- HPMC viscosity and solvent systems investigated

Morphologies linked to phase behaviour and material properties

Drop tube – in place

Material properties – AFM technique explored

Model of bubble expansion (no drying) within a droplet developed and simulated

2 Drying at High Temperature

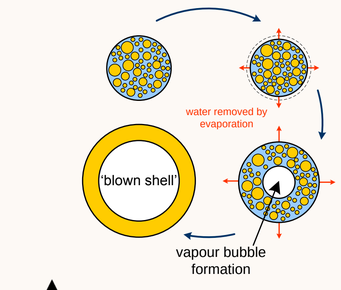

Bubble nucleation leads to mechanical deformation, puffing, and very significant changes in physical and functional properties

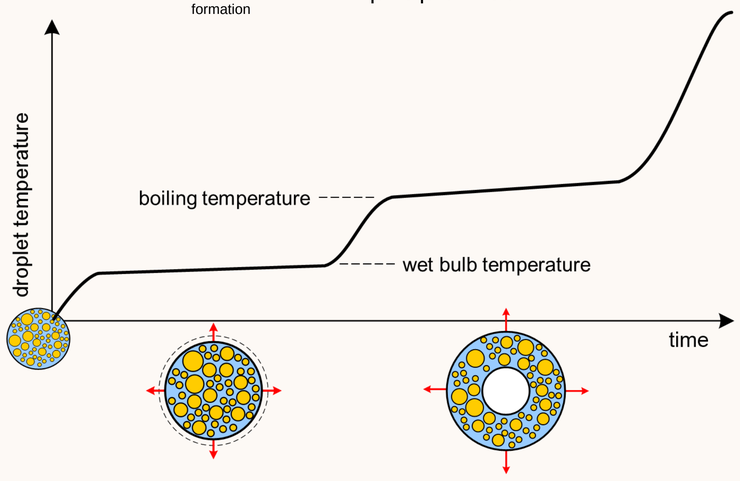

3 Filament Drying Rig

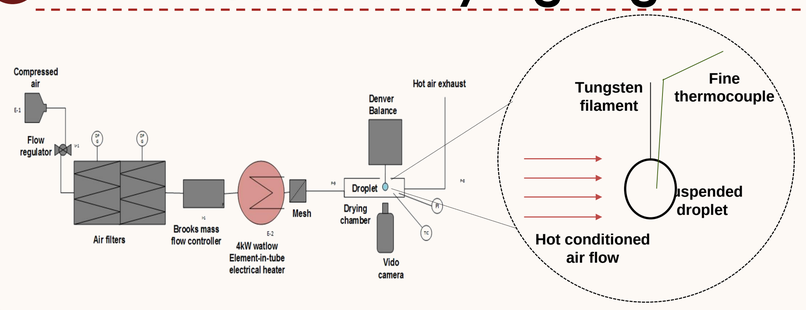

4 Morphology evolution of sodium silicate

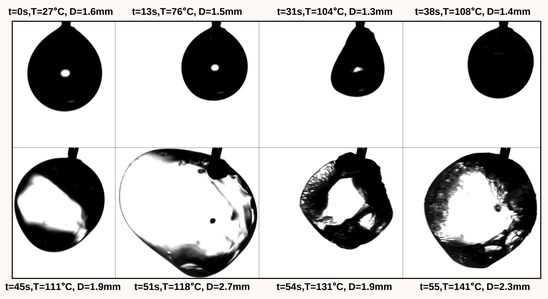

Drying of Sodium silicate droplet
$D_{initial}$ =1.6 mm
$C_{initial}$ = 15%
T_{air} = 180°C
Drying progress: Inflation and puffing

5 Drying mechanisms

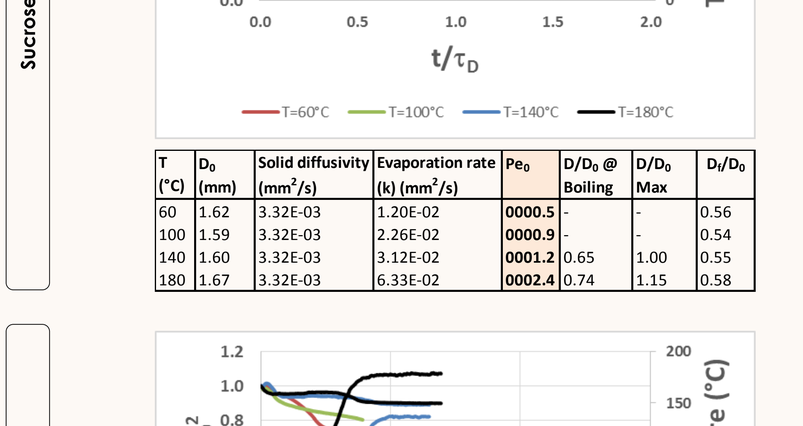

6 Drying kinetics (5% w/w)

Sucrose

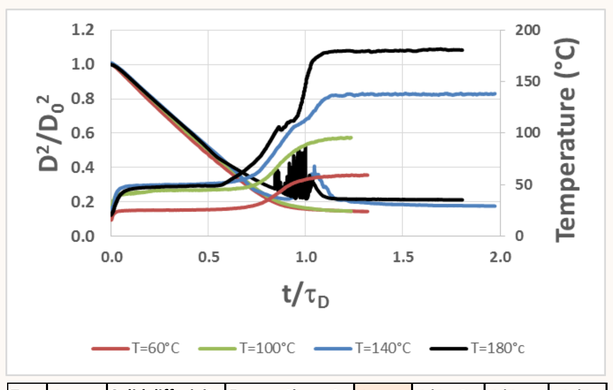

T (°C)	D_0 (mm)	Solid diffusivity (mm^2/s)	Evaporation rate (k) (mm^2/s)	Pe_0	D/D_0 @ Boiling	D/D_0 Max	D_f/D_0
60	1.64	3.32E-03	1.20E-02	**0000.5**	-	-	0.38
100	1.75	3.32E-03	2.16E-02	**0000.8**	-	-	0.38
140	1.57	3.32E-03	3.36E-02	**0001.3**	0.46	1.00	0.42
180	1.63	3.32E-03	5.58E-02	**0002.1**	0.53	1.00	0.46

HPMC

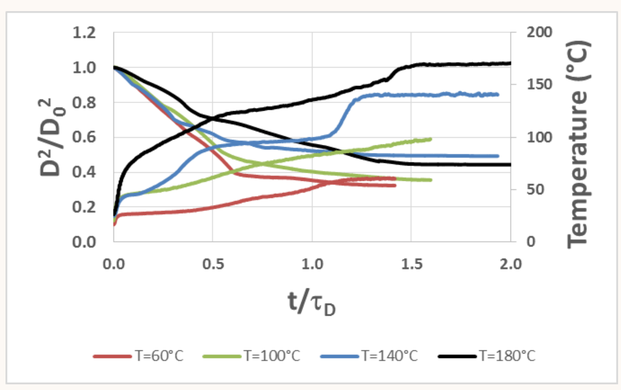

T (°C)	D_0 (mm)	Solid diffusivity (mm^2/s)	Evaporation rate (k) (mm^2/s)	Pe_0	D/D_0 @ Boiling	D/D_0 Max	D_f/D_0
60	1.64	2.93E-06	1.10E-03	**0046.9**	-	-	0.57
100	1.75	2.93E-06	1.90E-02	**0809.7**	-	-	0.60
140	1.57	2.93E-06	3.01E-02	**1282.7**	0.72	1.00	0.70
180	1.63	2.93E-06	3.51E-02	**1495.8**	0.91	1.00	0.67

Sodium silicate

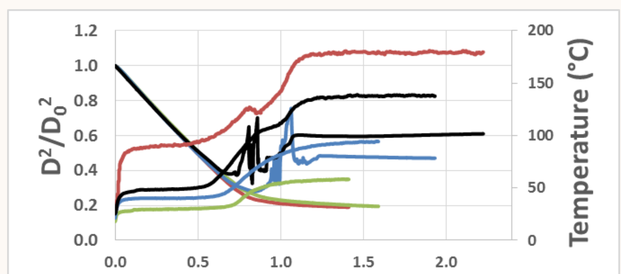

T (°C)	D_0 (mm)	Solid diffusivity (mm^2/s)	Evaporation rate (k) (mm^2/s)	Pe_0	D/D_0 @ Boiling	D/D_0 Max	D_f/D_0
60	1.64	1.96E-04	1.11E-02	**0007.1**	-	-	0.44
100	1.75	1.96E-04	2.22E-02	**0014.2**	-	-	0.69
140	1.57	1.96E-04	3.38E-02	**0021.5**	0.53	1.00	0.44
180	1.63	1.96E-04	4.71E-02	**0030.0**	0.62	1.00	0.78

7 Drying kinetics (15% w/w)

Sucrose

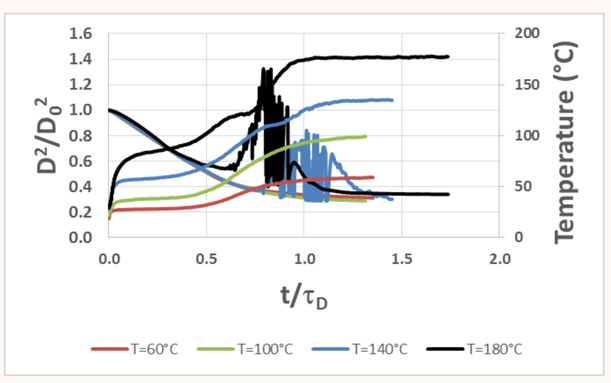

T (°C)	D_0 (mm)	Solid diffusivity (mm^2/s)	Evaporation rate (k) (mm^2/s)	Pe_0	D/D_0 @ Boiling	D/D_0 Max	D_f/D_0
60	1.62	3.32E-03	1.20E-02	**0000.5**	-	-	0.56
100	1.59	3.32E-03	2.26E-02	**0000.9**	-	-	0.54
140	1.60	3.32E-03	3.12E-02	**0001.2**	0.65	1.00	0.55
180	1.67	3.32E-03	6.33E-02	**0002.4**	0.74	1.15	0.58

HPMC

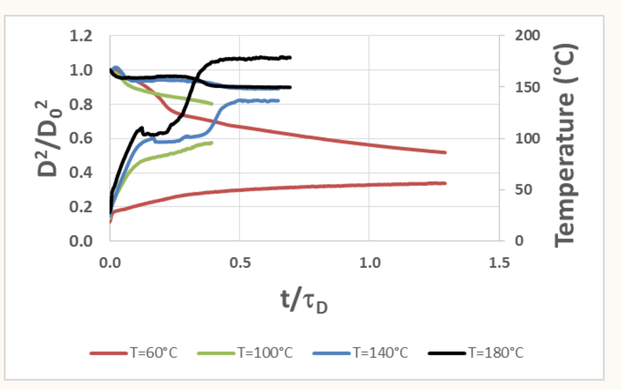

T (°C)	D_0 (mm)	Solid diffusivity (mm^2/s)	Evaporation rate (k) (mm^2/s)	Pe_0	D/D_0 @ Boiling	D/D_0 Max	D_f/D_0
60	1.57	2.69E-07	7.70E-03	**3579.8**	-	-	0.72
100	1.45	2.69E-07	4.70E-03	**2185.0**	-	-	0.90
140	1.57	2.69E-07	1.09E-02	**5067.4**	0.97	1.00	0.94
180	1.50	2.69E-07	1.73E-02	**8042.8**	0.98	1.00	0.95

Sodium silicate

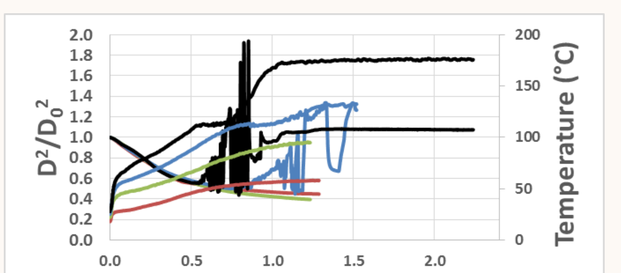

T (°C)	D_0 (mm)	Solid diffusivity (mm^2/s)	Evaporation rate (k) (mm^2/s)	Pe_0	D/D_0 @ Boiling	D/D_0 Max	D_f/D_0
60	1.49	1.96E-04	9.70E-03	**0006.2**	-	-	0.67
100	1.55	1.96E-04	2.04E-02	**0013.0**	-	-	0.63
140	1.72	1.96E-04	3.06E-02	**0019.5**	0.75	1.16	1.23
180	1.63	1.96E-04	4.07E-02	**0025.9**	0.71	1.50	1.40

8 Final morphologies of HPMC

Single particles from filament rig

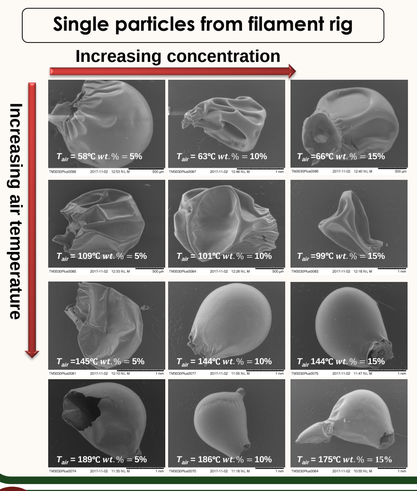

Spray dried particles (10% w/w)

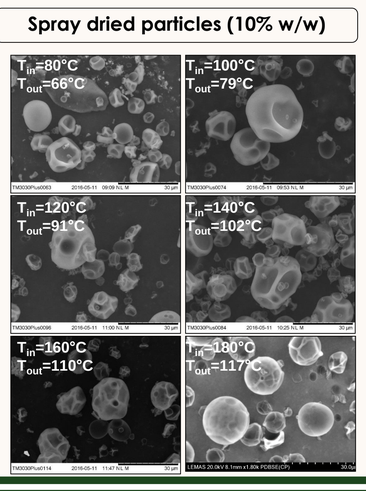

9 Phase changes during drying

Concentration vs temperature drying trajectory of 15% w/w HPMC droplet at 200°C air temperature superimposed on HPMC phase diagram

Droplet crosses phase boundaries into regions with different material properties

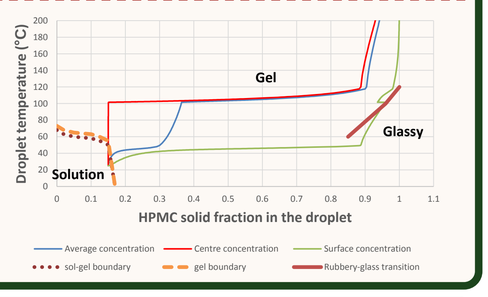

11 2D bubble expansion

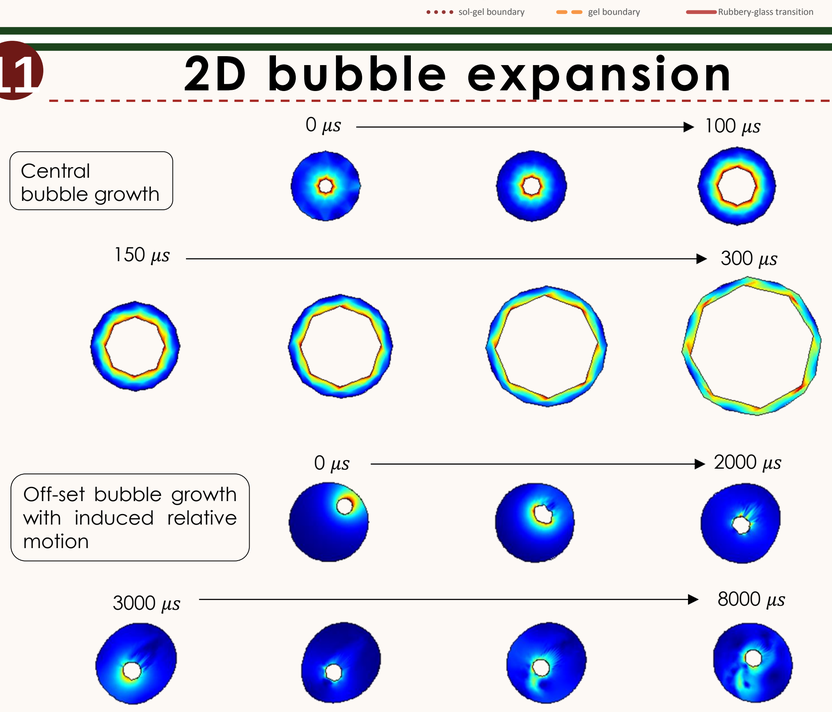

10 Modelling Morphology Evolution

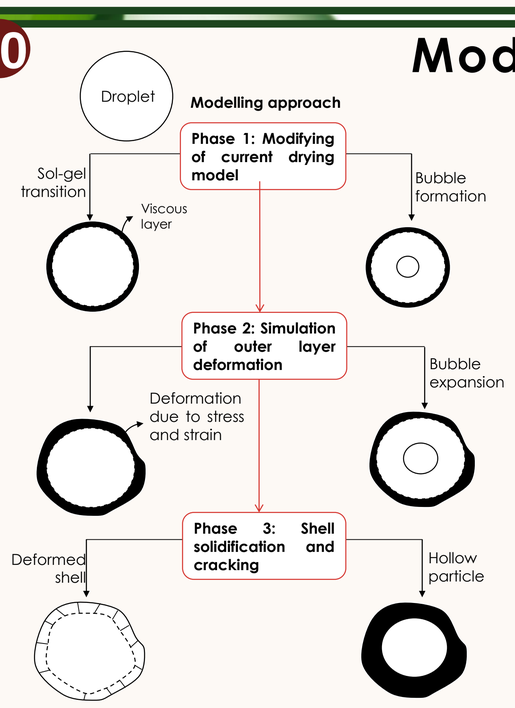

Bubble Expansion Model (no drying)

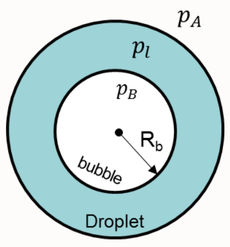

Approaches
- 1-D (spherically symmetric) - Modified Rayleigh-Plesset eqn
- Finite Volume (Fluent) - 2/3D VOF
- Finite Element (Comsol) - 2/3D ALE

FEM model:
- Oscillating bubble size and pressure
- 200 um bubble in 1 mm droplet
- Initial bubble pressure 5KPa

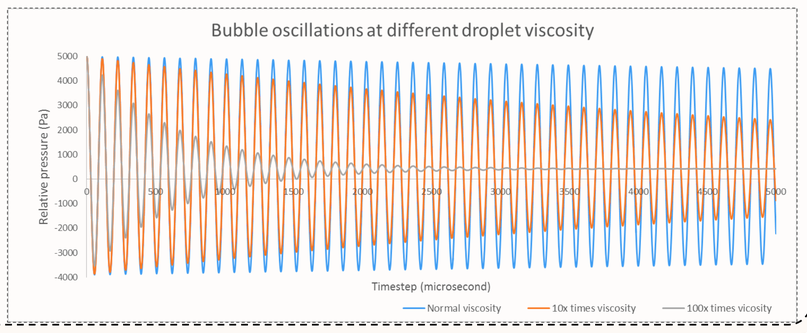

12 Summary and Future Plan

- Robust method for quantitatively assessing drying kinetics and morphology development
- Morphology driven by material property differences at low % H20 and high T
- Regime map by rationalising exp. data with 1-D drying model

Future experimental: comparison with drop tube, droplet mass

- Modelling – bubble expansion allows exploration of system
- Future modelling – coupling with drying

Acknowledgements

- Prof. Phil Threfall Holmes, Prof. Nik Kapur
- Leeds technicians
- Funding also received from EPSRC and the University of Leeds

Nonlocal Rheology of Granular Flows

Zhu Tang* Karen Daniels* Jonathan Kollmer*§ Ted Brzinski*¤ Michael Shearer* Nathalie Vriend# Amalia Thomas#

*NC State §Duisberg-Essen ¤Haverford #Cambridge

IFPRI International Fine Particle Research Institute

NC STATE UNIVERSITY

Problem Statement

- There is no first-principles, general theory of intermediate granular flow that predicts the rheological response as a function of particle size/shape/friction
- Currently: use empirical relations fit to bulk data for that particular flow geometry and particles
- Needed: An improved understanding of how **particle properties** control the rheology of granular materials, independent of geometry

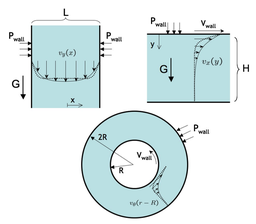

Kamrin & Koval. PRL (2012)

Local Rheology

- inertial number: ratio $I = \frac{\dot{\gamma} d}{\sqrt{P/\rho}}$ between
  - micro timescale T to squeeze a particle into a hole
  - macro timescale ($1/\dot{\gamma}$) of deformation
  - large I corresponds to rapid flow

density ρ
diameter d

- stress ratio $\mu = \frac{\tau}{P}$ between
  - shear stress
  - normal pressure

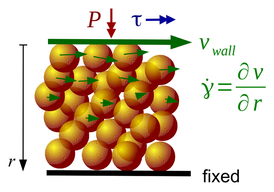

Nonlocal Rheology (Cooperative Model)

- define granular fluidity: $g \equiv \dot{\gamma}/\mu$
  - macroscopic susceptibility of a granular region to flow
- locally, model the granular material as a Bingham fluid:

$$g_{loc} = \frac{\dot{\gamma}_{loc}}{\mu} \approx \sqrt{\frac{P}{\rho d^2}} \frac{\mu - \mu_s}{b\mu} \; for \; \mu > \mu_s \qquad (0 \; for \; \mu \le \mu_s)$$

  - μ_s: incipient yield stress ratio (Coulomb failure)
  - b: sets magnitude of local fluidity
- fluidity is determined by both local fluidity and a non-local, cooperative effect (beyond Bagnold scaling):

$$g = g_{loc} + \xi^2 \nabla^2 g$$

- the cooperative length scale ξ is set by
  - A: controls of strength of cooperativity

$$\frac{\xi}{d} = A\sqrt{\frac{1}{|\mu - \mu_s|}}$$

[measured values]
[model parameters]

How do μ_s, A, b depend on particle properties?

Three Ways of Determining μ_s

- upper limit of slowest $\mu(I)$ curve: $\mu_s > 0.26$
- maximum of $\xi(\mu)$: $\mu_s \sim 0.26$
- force chain fluctuations: $\mu_s < 0.29$

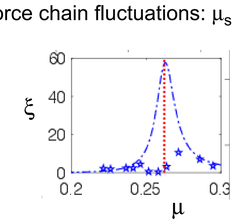

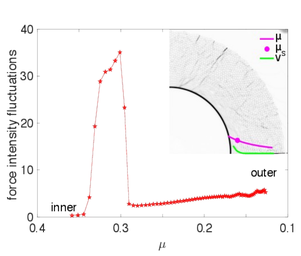

Testing Shape-Dependence

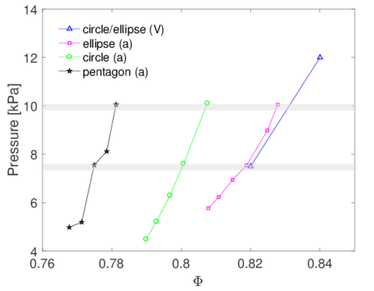

- New laser-cut shapes
  - acrylic: stiffer (3 GPa) than Vishay (0.2 GPa)
  - chosen to be round vs. anisotropic vs. angular
  - central hole for ease of tracking
- select appropriate # of particles to achieve two selected values of pressure (7.5 and 10 kPa)

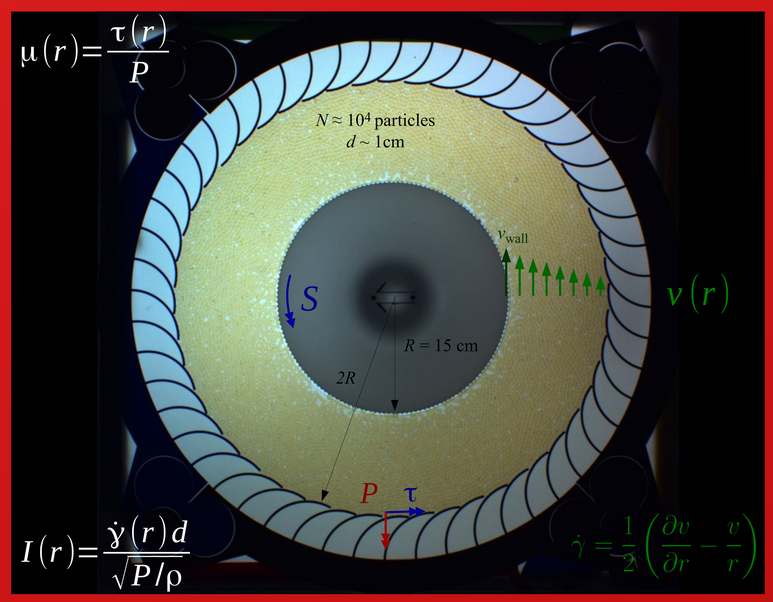

Success of Nonlocal Rheology

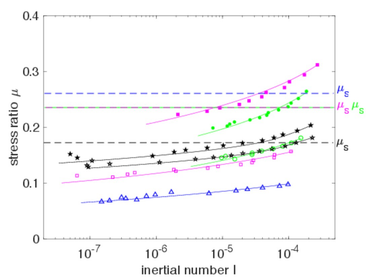

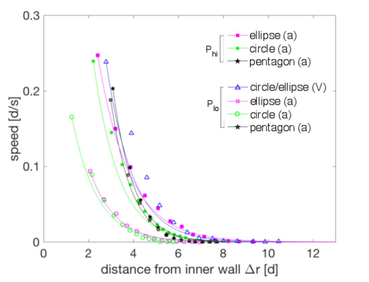

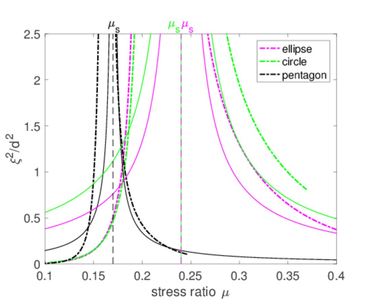

- Collect data in both the local and nonlocal regimes, with the P = 7.5 kPa runs crossing μ_s
- Nonlocal rheology is able to capture $\mu(I)$, as was previously observed at various shear rates and packing fractions
- Provides good agreement with all velocity profiles
- All experiments done with an inner wall rotation rate of 1.3 d/s (not captured by camera)
- Nonlocal cooperative length ξ is observed to diverge at the same μ_s obtained from slow-rotation runs.
- Legend: solid = model, dashed = experiments

Effect of Particle Properties

	Vishay circles/ellipses	acrylic ellipses	acrylic circles	acrylic pentagons
μ_s	0.26 ± 0.02	0.24 ± 0.02	0.24 ± 0.02	0.17 ± 0.01
b	1.1 ± 0.3	1.1 ± 0.5	1.1 ± 0.6	1.1 ± 0.6
A	0.402 ± 0.003	0.231 ± 0.003	0.280 ± 0.003	0.101 ± 0.001

- μ_s (yield stress ratio)
  - determined from slow-shear experiments, consistent with calculated $\xi(\mu)$ curves
  - shape-dependent for same material
- b: local parameter
  - determined by fitting $\mu(I)$ to P = 7.5 kPa data
  - insensitive to material, shape
- A: nonlocal parameter
  - determined by fitting $\mu(I)$ to P = 7.5 kPa data
  - sensitive to both shape and material

Local Interpretation of Fluidity?

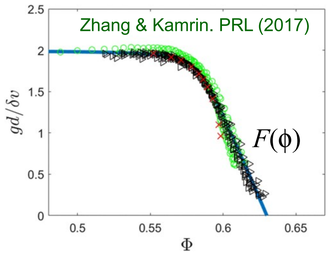

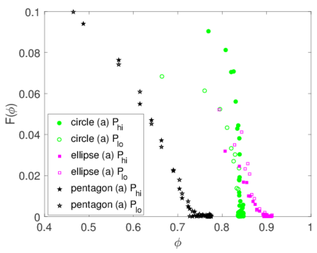

- Prediction: fluidity g determined by universal function $F(\phi)$
  - $g = \frac{\delta v}{d} F(\phi)$
- Observation: $F(\phi)$ is shape-dependent
  - round particles may be affected by crystallization at higher pressures

Conclusions

- can determine a set of nonlocal model parameters for each set of particles → reuse at different flow speeds, pressures
  - each set of parameters successfully fits $\mu(I)$, $v(r)$, $\xi(\mu)$
- first nonlocal rheology experiments as a function of particle properties
  - begin to identify which model parameters are associated with which particle properties
  - particle-scale fluidity is no longer a universal function
- **Renewal:** experiments to determine generalizations for predetermining boundary conditions
- **Ultimately:** predict parameters for given shape/size/roughness/stiffness; use with boundary conditions to quantitatively predict flows
- **Collaboration**: with Nathalie Vriend, testing nonlocal rheology in intermediate chute flows using photoelastic particles; make connections between nonlocality and μ_s fluctuations

References

- Kamrin & Koval. *Physical Review Letters.* 108:178301 (2012)
- Zhang & Kamrin. *Physical Review Letters.* 118: 058001 (2017)
- Tang, Brzinski, Shearer, Daniels. *Soft Matter.* 14: 3040-3048 (2018)

Non-local effects in intermediate flows

A.L. Thomas [1], Z. Tang [2], K.E. Daniels [2], N.M. Vriend [1] (nv253@cam.ac.uk)

[1] DAMTP, University of Cambridge, UK, [2] Physics, North Carolina State University, USA

1 Photoelasticity

Using birefringent particles to measure stresses [1]:
- Stresses change polarization of transmitted light
- Calibration between optical pattern and applied force

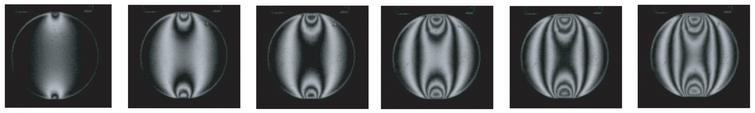

Novelty of our method:
- Custom-made high-quality particles following [2], virtually stress-free
- Dynamic interactions [3] during loading and unloading in milliseconds

→ No force equilibrium exists!

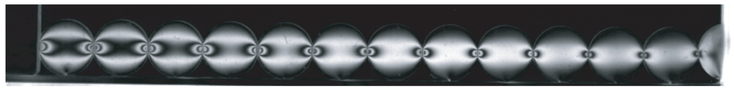

Potential and impact:
- Non-local effects and rheology in intermediate inertial number flows

2 Experimental set-up

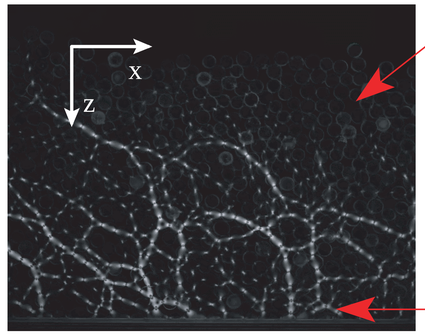

Optical 2D avalanche chute with acrylic walls
- 20 - 30s continuous avalanches with constant height and flux
- Inclined at 20 degrees, at a flux of Q = 0.0564 m²/s, at 0.25m from outlet
- Using two opposite polarized films and a high-speed camera (1000 fps)
- Flows with particles of diameter 1.1 - 1.3 cm
- Alternating frictional base

Flowing

Intermediate flow regime → inertial number I up to:

$$I = \frac{\dot{\gamma} d}{\sqrt{P/\rho}} \approx 0.25$$

Quasi-static

1. Detection limit: → F > 0.01 N
2. Hydrostatic pressure increase with depth
3. Coarse-graining length → 3*D

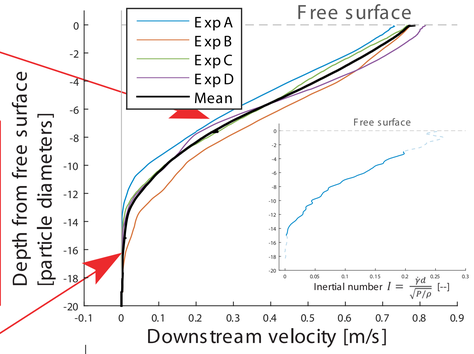

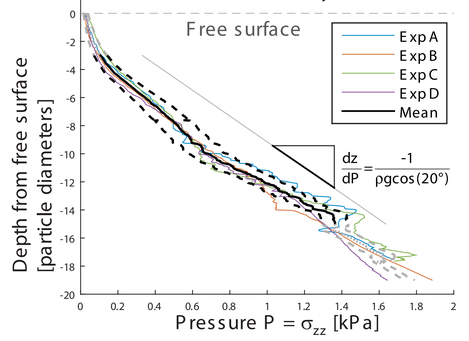

3 Data analysis

Stress tensor components:
- Hydrostatic pressure increase:

$$\sigma_{zz} = (h - z)\rho g cos(\theta)$$
$$\sigma_{zx} = (h - z)\rho g sin(\theta)$$

- Symmetry in normal stresses
- Asymmetry in shear stresses:

→ rotation?

- Stress ratio:

$$\mu = \frac{\sigma_{xz}}{\sigma_{zz}}$$

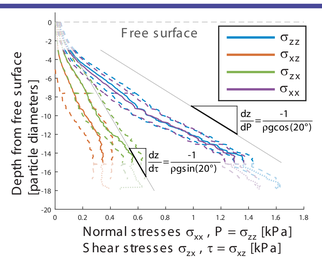

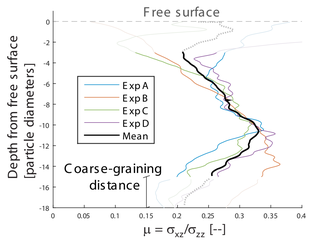

Fluctuations of pixel intensity I:

$$I'(x,z,t) = I(x,z,t) - \langle I(x,z,t)\rangle_t$$

- Method 1: velocity fluctuations

a. Standard deviation in time:

$$\delta I(x,z) = \sqrt{\langle I'^2(x,z,t)\rangle_t}$$

b. Mean value over x: $\delta I(z) = \langle \delta I(x,z)\rangle_x$

- Method 2: temporal decorrelation

a. Autocorrelation of intensities at lag k:

$$r(x,z,k) = \frac{\sum_{t=1}^{N_t-k} I'(x,z,t)I'(x,z,t+k)}{\sum_{t=1}^{N_t} I'(x,z,t)^2}$$

b. Exponential fit to get decorrelation time τ:

$$r_k = Ce^{-k\tau}$$

c. Mean value over x: $\tau(z) = \langle \tau(x,z)\rangle_x$

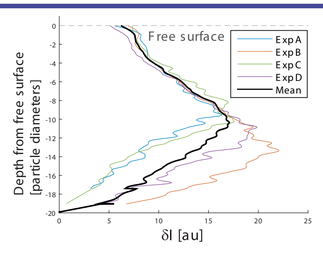

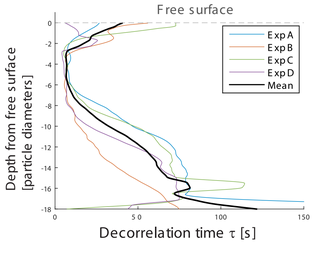

4 Nonlocal rheology

Explore correlation between:
- Stress ratio μ(z) and velocity fluctuations δI(z)
- Granular fluidity g(z): $g = \frac{\dot{\gamma}}{\mu}$

& temporal decorrelation time τ(z)

→ Non-local parameters [4,5]?

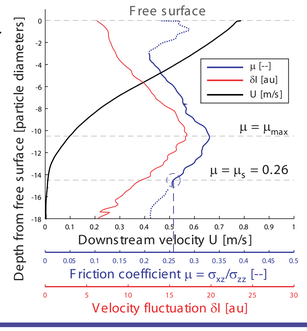

Highly correlated: correlation coefficient 0.967

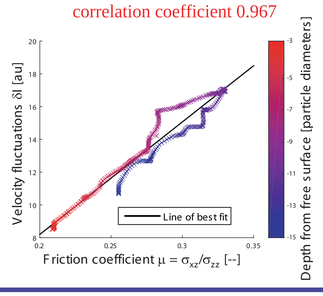

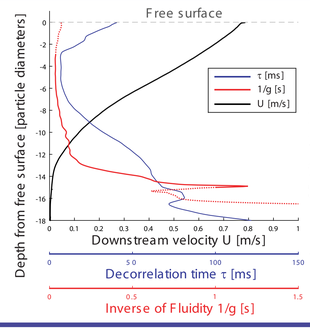

Highly correlated in two distinct regions

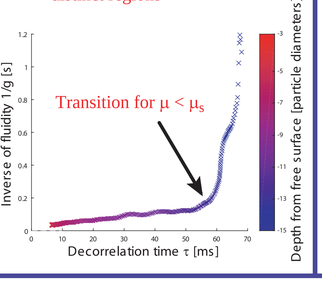

5 Conclusions

In this work we showed that photoelastic analysis allows the quantification of rheologies in an intermediate chute flow. We characterize stresses and velocities in a flow layer with regions below and above the yield ratio μ_s. We compare our experimental results with a nonlocal rheology. Preliminary results show that the timescale over which the force chains decorrelate is strongly associated with the inverse of the fluidity, a viscosity-like quantity. This provides a physical interpretation of its particle-scale origins.

Acknowledgements

This work was made possible by the support of an IFPRI collaborative grant. We thank Jonathan Bares for initial guidance on casting photoelastic particles and Jonathan Kollmer for the development of the code PEGS for dynamic applications. We are grateful to technicians David Page-Croft, Paul Mitton, Colin Hitch, Andrew Denson and John Milton for their invaluable help and technical support in the construction and maintenance of the experimental apparatus. NMV is supported by a Royal Society Dorothy Hodgkin Research Fellowship RG 70273, ALT is funded by a Royal Society Research Grant RG 73329 and the Cambridge International Trust and KED acknowledges support from the James S. McDonnell foundation.

References

[1] K.E. Daniels, J.E. Kollmer and J.G. Puckett, Rev. Sci. Instrum. 88, 051808 (2017).
[2] M. Cox, D. Wang, J. Barés, R. Behringer, EPL 115, 64003 (2016).
[3] Photoelastic disk solver (PEGS) available at https://github.com/jekollmer/PEGS
[4] K. Kamrin and G. Koval, Phys. Rev. Lett. 108, 178301 (2012).
[5] Z. Tang, T.A. Brzinski, M. Shearer, K.E. Daniels, Soft Matter 14, 3040-3048 (2018).

Effect of Solvents on Crystal Shape & Growth Kinetics

C. J. Tilbury and M. F. Doherty

Department of Chemical Engineering, University of California, Santa Barbara, CA

Abstract

"The goal of this research is to develop a practical engineering tool for predicting the relative growth rates (growth kinetics) and morphology of solution-grown faceted crystals, including the effects of solvent (Phase 1 of the research), and impurities/ additives (Phase 2)."

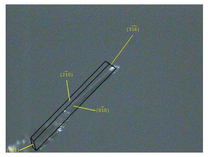

Adipic acid vapor growth
shape = rod/needle

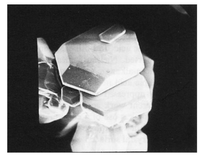

Adipic acid grown from water
shape = hexagonal platelet
(image from Davey et. al. 1992)

Motivation: Morphology control is important for processing & product functionality

Conventional models not reliable or predictive

Lovastatin

AE shape

Experimental growth shape

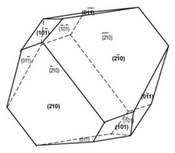

Figure 28. The attachment energy morphology of lovastatin.

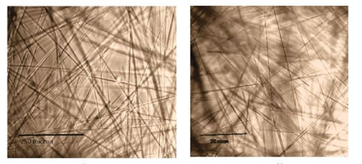

Figure 27. The experimental steady-state morphology of lovastatin grown from (a) isopropanol, (b) methanol.

Motivation: Develop a better approach based on growth mechanisms

Multiscale Mechanistic Framework

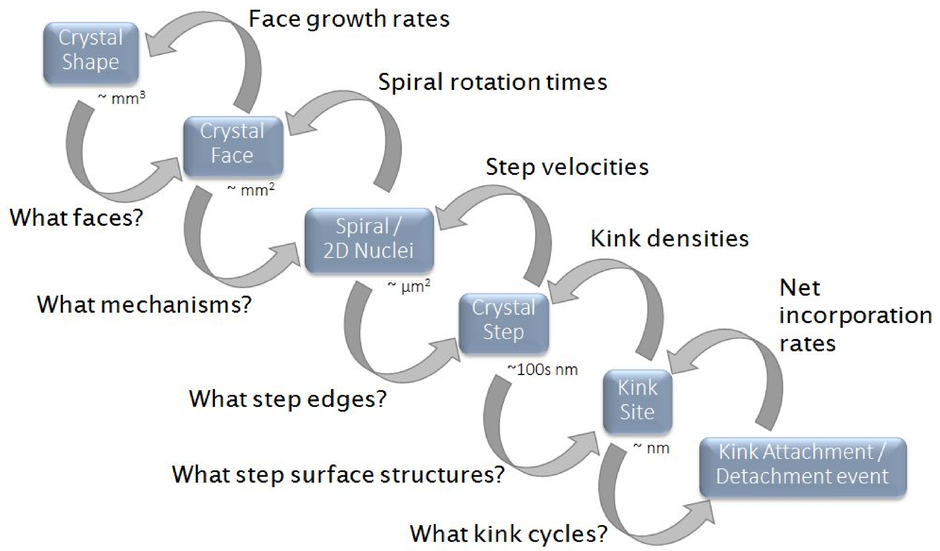

Olanzapine

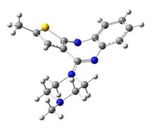

Olanzapine molecule

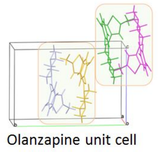

Olanzapine unit cell

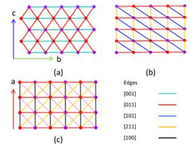

Olanzapine bond chains by face

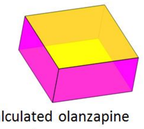

Calculated olanzapine vapor shape

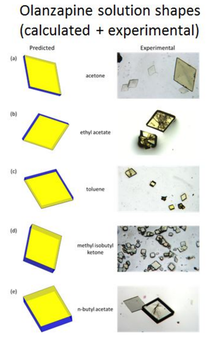

Lovastatin Revisited

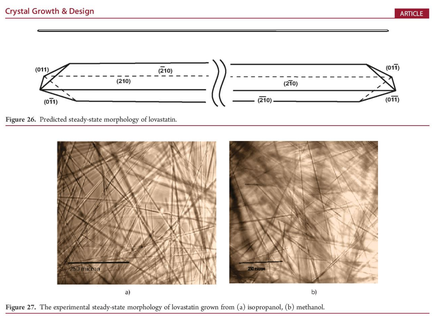

Figure 26. Predicted steady-state morphology of lovastatin.

Figure 27. The experimental steady-state morphology of lovastatin grown from (a) isopropanol, (b) methanol.

The New Frontier – Absolute Growth Rates

(not part of IFPRI project)

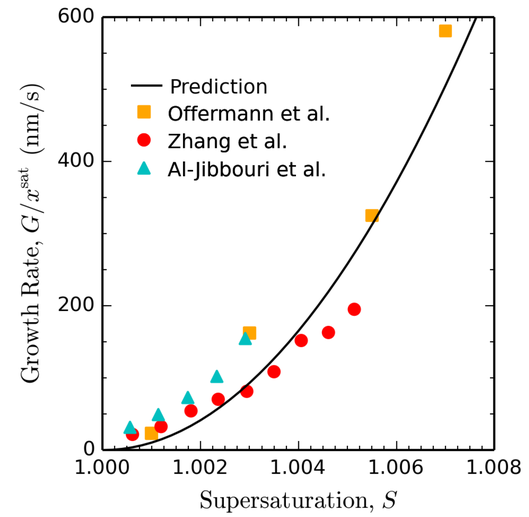

Conclusion: ***Absolute growth rate predictions & reliable morphology predictions will ONLY be possible using microscopic mechanistic models***

Mixing Rules for Powder Mixing (Phase 1): A PEPT Investigation of a Binary Mixture

Indresan Govender[1,2], Suren Moodley[1], Marcelle Pillay[1], Malcom Rengasamy[1]

[1]Chemical Engineering, University of KwaZulu-Natal, Glenwood, Durban, South Africa, 4041

[2]Chemical Engineering, University of Cape Town, Rondebosch, Cape Town South Africa, 7701

INTRODUCTION & BACKGROUND

The lack of fundamental understanding of mixing is intimately coupled to the lack of a universally valid granular flow theory. A compounding factor relates to the rich coexistence of flow regimes encountered in typical industrial granular flows that simultaneously exhibit solid-, liquid- and gas-like behaviour. The problem in realising a universally valid granular flow theory is strongly related to the difficulty in measuring (across the entire phase space pertinent to industrial flows):

a) Solid volume fraction distributions,

b) Detailed velocity fields and the associated shear rate, and

c) Stress fields.

Unfortunately, most measurements of granular flows lack sufficient detail and coverage of the phase space to yield universally valid results. Positron Emission Particle Tracking (PEPT) is arguably the most accurate and detailed measurement tool for determining (a) and (b). To determine the stresses requires a constitutive choice in the absence of direct stress measurements.

POSITRON EMISSION PARTICLE TRACKING (PEPT)

Drive system

Laboratory Drum

PEPT Scanner

PEPT PROCEDURE

Triangulation

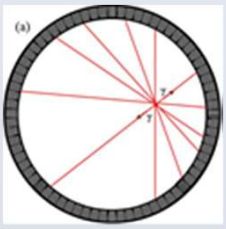

(x, y) trajectory

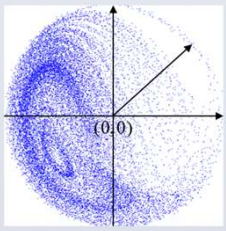

(z, y) trajectory

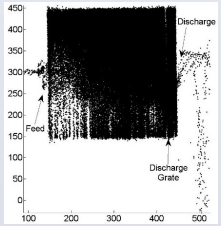

Triangulation of the gamma rays emanating from the radiolabeled particle (3mm or 5mm plastic bead) results in 3D trajectories (x, y, z, t) of the tracer—the raw data from PEPT. Timing resolution of PEPT scanner is typically a few milliseconds which is ideal for meso-scale granular flow modelling.

Granular Rheology from PEPT Data

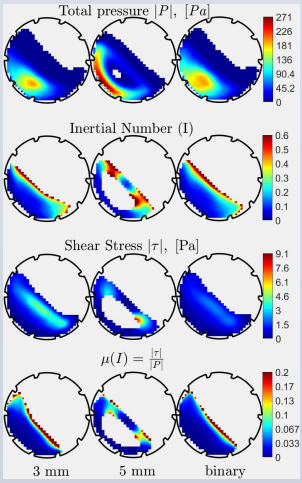

48.8 rpm

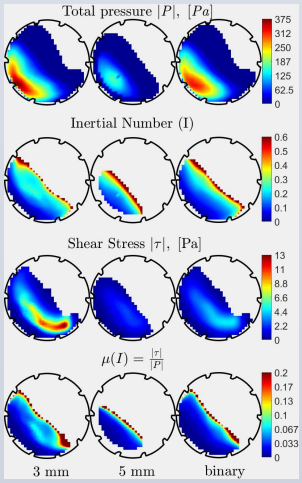

73.3 rpm

EXPERIMENTAL CONFIGURATION & ANALYSIS

Across 4 fill fractions (10%, 20%, 30%, 40%), a mixture of 3 and 5 mm particles (split equally by mass) was operated at 40, 60, 70, 80, 90, 100, and 110% of critical speed. The 3 and 5 mm particles had to be tracked separately for each configuration. By the ergodic hypothesis, the time averaged data per spatial voxel was recast into the ensemble average to yield the key ingredients for understanding mixing and granular flow. A typical illustration of the calculations for the 40% load at 40% and 60% of critical speed is given below.

40% of critical Speed (48.8 rpm)

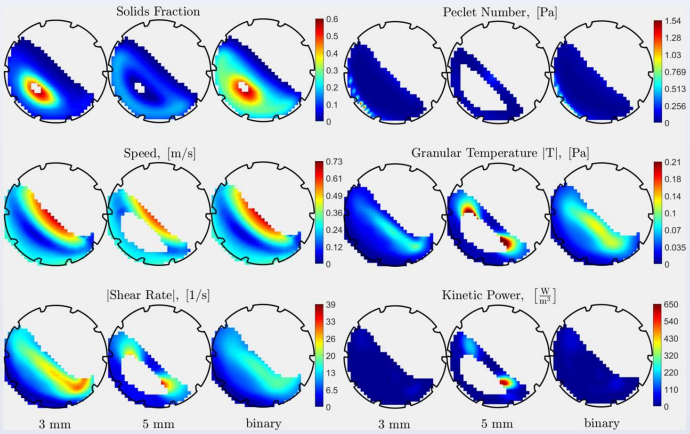

60% of critical Speed (73.3 rpm)

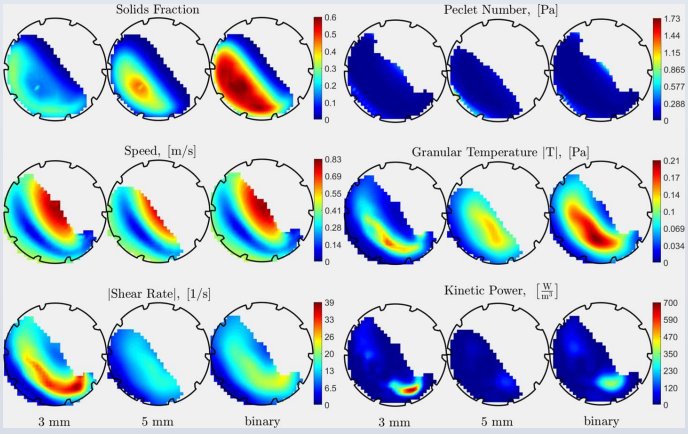

INITIAL FINDINGS

1. Th solids fraction maps suggest that the kinetic stress theory reverses from 40% to 60% critical speed.
2. The shear rate and shear stress is maximum near the toe region for the 60% speed.
3. For the lower speed, the shear stress and shear rate is spread uniformly along a thin layer near free surface.
4. Velocity fluctuations appear highest in the central region of the bed, with the 60% speed depicting an overall higher granular temperature.
5. The effective friction (μ)—a proxy for flow energy dissipation—is highest in the thin flow layer, dropping exponentially deeper within the bed.
6. The rising layer depicts very low effective friction values suggesting a more solid-body-like motion.
7. The pressure dominates over the shear stress by an order of magnitude.
8. Kinetic Power dissipation is higher for the higher speed, and concentrated near the toes region.
9. The range of Peclet number suggests both diffusive & convective mass transfer, albeit that most of the bed appears to be diffusion dominated.

ACKNOWLEDGEMENTS

A special thanks to the Center for Minerals Research (CMR) laboratory staff for assisting with PEPT experiments.

3D Printed "Perfect Particles"

Ruihuan Ge[1], Mojtaba Ghadiri[2], Tina Bonakdar[2], Zongyan Zhou[1], Ian Larson[3] & Karen Hapgood[1,4]

[1]Chemical Engineering, Monash University [2]Institute of Particle Science and Engineering, University of Leeds

[3]Monash Institute of Pharmaceutical Sciences, Monash University [4]School of Engineering, Deakin University

1. Introduction

- Test agglomerates with controlled structure and "tuneable" properties are needed to validate simulation models.
- Agglomerates with defined and tuneable properties were produced using 3D printing technology. 1) Cubic tetrahedral structure 2) Spherical random structure
- Rigid primary particles (d_p= 4mm) connected by cylindrical inter particle bonds (ductile DM 9895 polymer)
- DEM breakage simulations with properties matching the 3D printed agglomerate were conducted and compared with experimental results.

Cubic tetrahedral structure (L_b =4.25 mm, r_b=1.3 mm)	Random structure (ε=49 %, L_b =4.25 mm, r_b=1.3 mm)	Dense structure (ε=44 %, L_b =4 mm, r_b=1 mm)
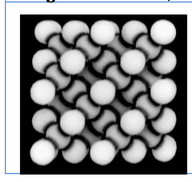	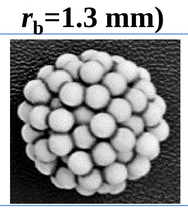	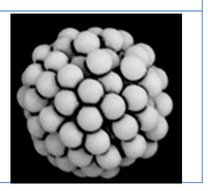

2. DEM Simulation & Experimental

- DEM simulations in EDEM used the TBBM model, where a beam connect the particle centres

➢ **Modified bond Young's modulus $E_{b,m}$**

- Initial results showed a large difference in results for the random structured agglomerate, due to non-linear bond behavior in the 3D printed agglomerate (TBBM assumes linear behavior)
- The bond Young's modulus E_b was measured via doublet compressions & corrected for geometry difference

Random spherical agglomerate (ε=44%) Quasi-static compression 0.02 mm/s.

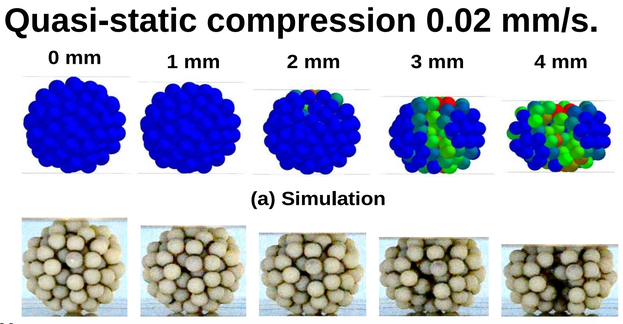

- Corrected bond Young's modulus $E_{b,m}$:

$$E_{b,m} = \frac{k_c \cdot L_b}{A_b}$$

k_c: Bond stiffness determined by doublet compression tests.
L_b : Bond length in TBBM model.
$A_b = \pi r_b^2$: Bond cross-sectional area.

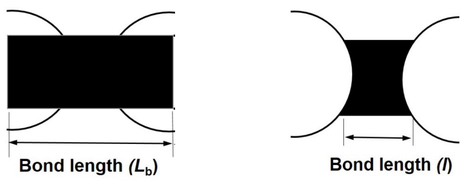

(a) TBBM (b) 3D printed

- FEM of doublet used to determine limit of *linear elastic* bond deformation (<1 mm):

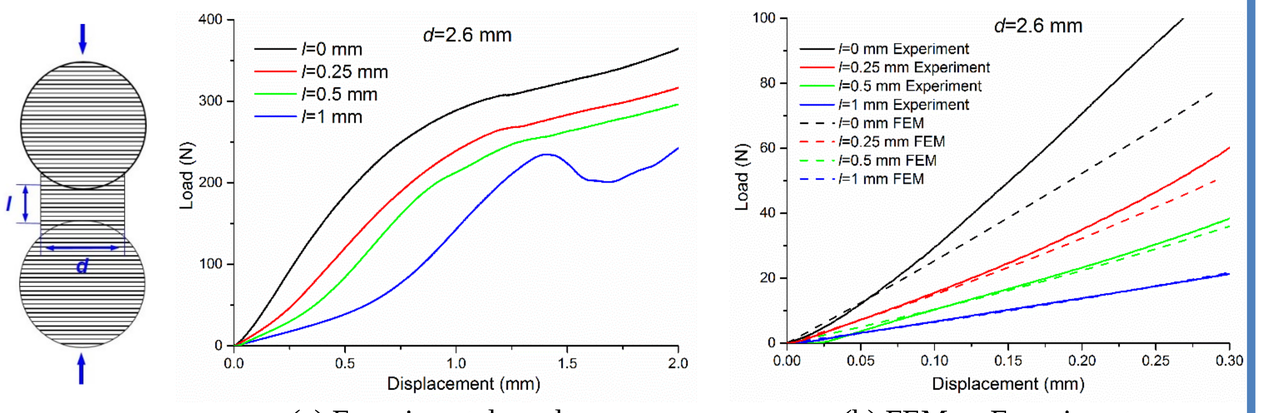

(a) Experimental results (b) FEM vs Experiment

Doublet force-displacement compression (perpendicular loading vs print) & FEM

3. Comparison of load-displacement curves

- A spherical random structure (ε =49 %) with same *average* bond length (L_b= 4.25 mm) as the cubic tetrahedral structure and same corrected bond Young's modulus $E_{b,m}$.
- Corrected bond Young's modulus $E_{b,m}$ captures the compressive load at the initial elastic stage (~1 mm deformation). Beyond this point, nonlinear behaviour takes over

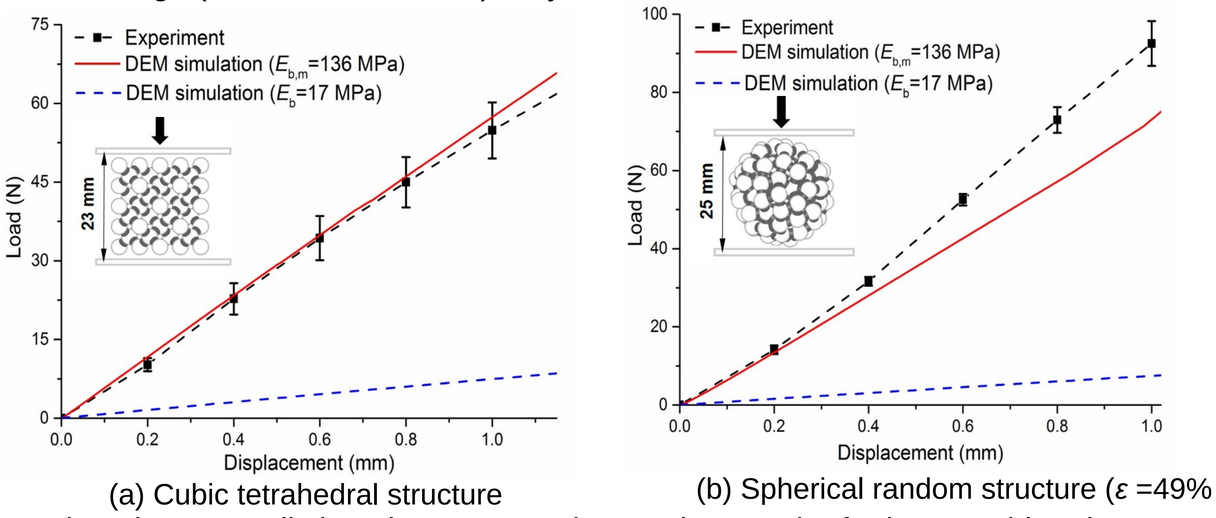

(a) Cubic tetrahedral structure (b) Spherical random structure (ε =49%

To make a better prediction, there are two issues that require further consideration:

- Non-linear and anisotropic characteristics of 3D printing materials.
- Non-linear contacts between particles when particles are in contact (l=0).

4. New uses for 3D printed particles: Flow of irregular particles

- Flow of irregular shaped particles. Testing of original shape and "equivalent" DEM shape in simple flow – how many spheres are required?

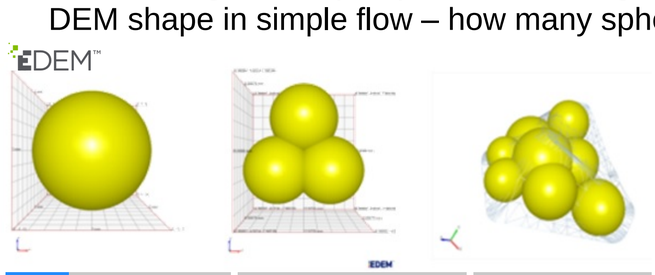

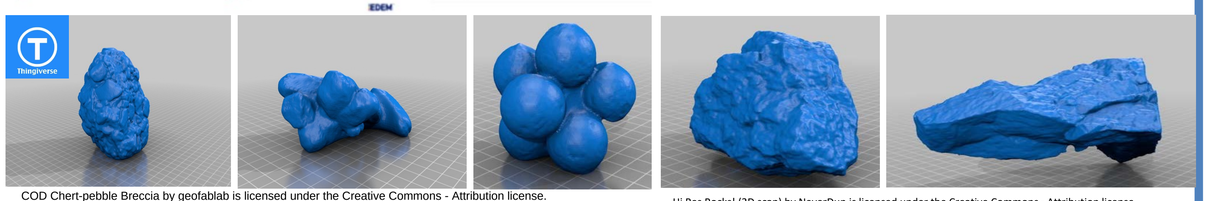

COD Chert-pebble Breccia by geofablab is licensed under the Creative Commons - Attribution license.

Hi Res Rocks! (3D scan) by NeverDun is licensed under the Creative Commons - Attribution license

ROCKY

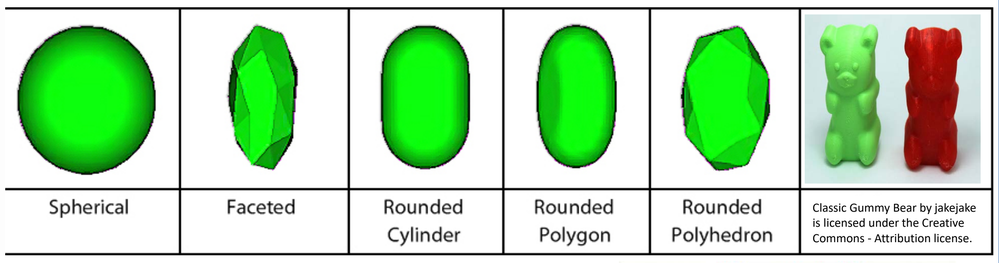

Classic Gummy Bear by jakejake is licensed under the Creative Commons - Attribution license.

- Use 3D printing colours for particle size and/or density

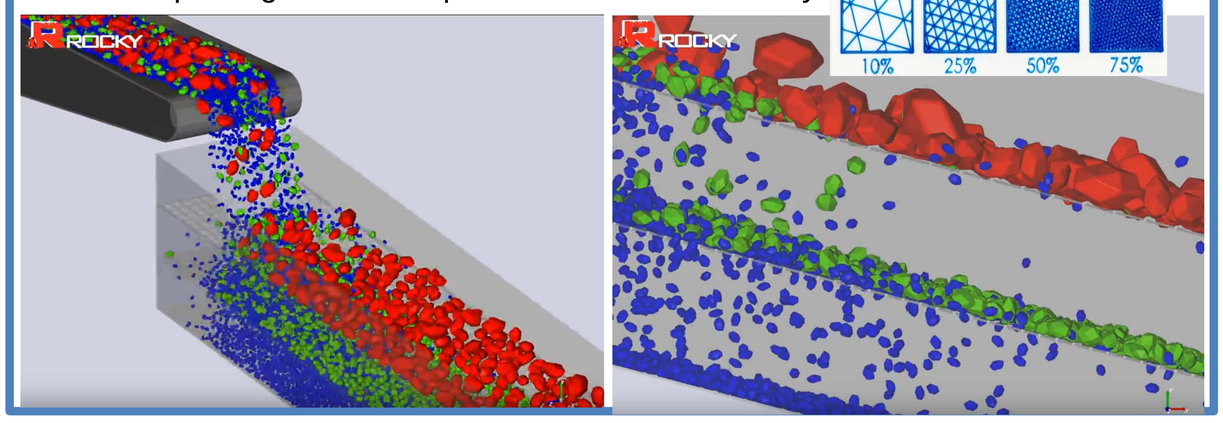

4. Binder Jetting printing

- *Extremely well controlled* agglomeration via drops – metals & other powders
- Similarities to wet granulation – drop penetration by a binder into powder bed
- *Screening criteria for a powder to be possibly suitable for 3D printing?*

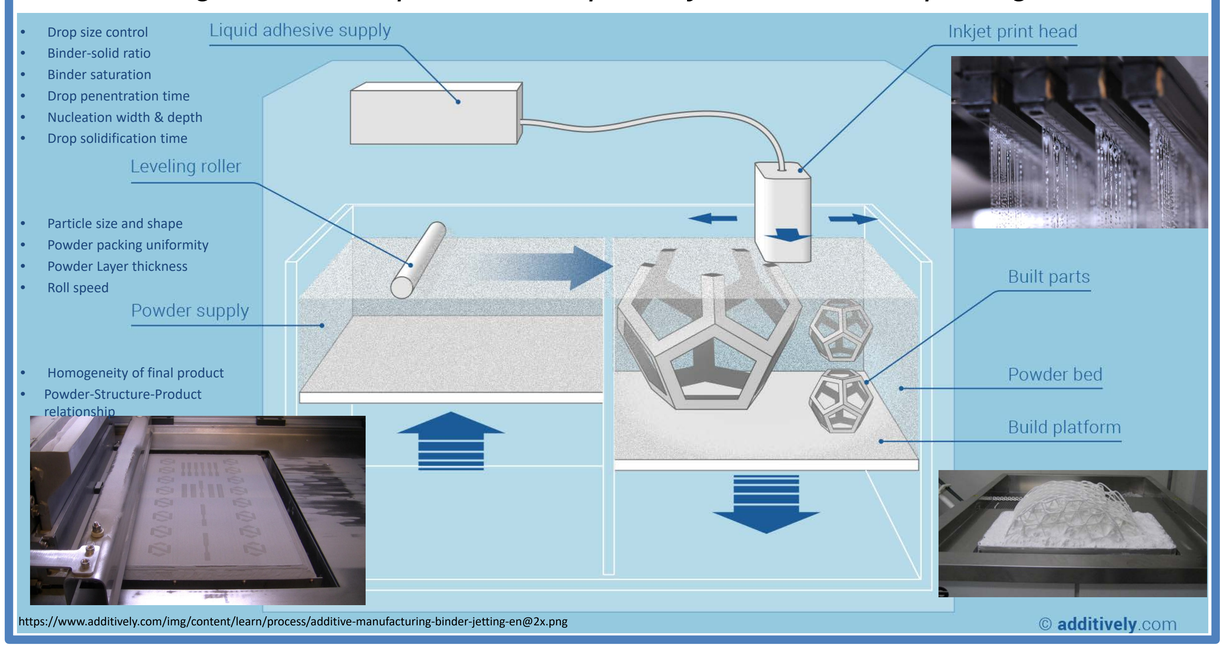

Summary

- Several agglomerates with defined structures & tunable bond properties were successfully 3D printed – able to conduct standard breakage tests
- Experimental breakage data compared with DEM simulations and showed qualitatively similar macroscopic breakage patterns.
- Quantitatively, DEM simulation using a newly developed TBBM bond model can predict the elastic deformation *(only)* of agglomerate structures.
- Non-linear behaviour is highly reproducible but not modelled
- Newer work underway on using 3D printed particles to test particle shape & density effects
- 3D Binder jetting project likely to build on existing IFPRI-funded work

Australian Government
Australian Research Council

International Fine Particle Research Institute

UNIVERSITY OF LEEDS

Flowability of Weakly Consolidated Powders

Colin Hare[1], Ali Hassanpour[2], Azza Mahmoud[1], Alexandros Stavrou[1]

[1]Department of Chemical and Process Engineering, Faculty of Engineering and Physical Sciences, University of Surrey, Guildford, Surrey, GU2 7XH, UK

[2]School of Chemical and Process Engineering, Faculty of Engineering, University of Leeds, Leeds, West Yorkshire, LS2 9JT, UK

1. Project brief

Measurement of unconfined yield strength of powders can be made with a variety of commercially available shear testing devices. Traditional flowability measurement devices have a number of short comings:

- Reproducibility of unconfined yield strength is greatly reduced at low stresses
- Or sometimes measurement is inconsistent with observed behaviour
- Materials found to be cohesionless may still have practical differences
- Generally the onset of flow is measured, which may not be a complete flow description

IFPRI seek to develop a theoretical understanding of flow of weakly consolidated and weakly cohesive powders

- Development of practical means of making measurement to support theory
- Results should be generalisable to a broad class of powders

2. Ball indentation

Ball indentation is a method for assessing powder flow under low stresses and varying strain rates that requires only a very small amount of material. The experimental procedure comprises of three steps:

- A powder bed is consolidated to a desired stress
- The powder bed is penetrated by a spherical indenter, until a desired penetration depth has been reached
- The indenter is unloaded

Flowability is determined by calculating hardness (Eq. 1), which represents flow stress and is the resistance of a material to plastic deformation, from the force-displacement response of the bed (Fig. 1). Provided that the bed does not consolidate, hardness can be linked to the unconfined yield strength, which is derived by the commonly used shear testers, via the constraint factor (Eq. 3), a material dependent property.

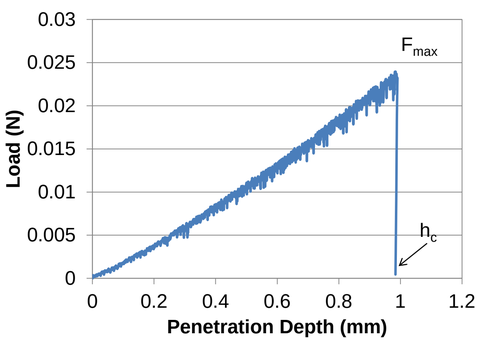

Figure 1. Force-displacement curve

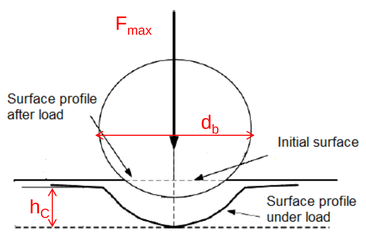

Figure 2. Bed surface profile

$$H = F_{max}/A \quad \textit{(Eq. 1)} \qquad A = \pi\left(d_b h_c - h_c^2\right) \quad \textit{(Eq. 2)} \qquad H = CY \quad \textit{(Eq. 3)}$$

3. Methods used

In the initial IFPRI project, for the ball indentation method the bed was first vertically consolidated prior to testing; ensuring the stress direction during consolidation and failure was the same, as is the case for the shear cell and uniaxial compression methods. However, constraint factor was determined by comparison of hardness measured by indentation and unconfined yield strength measured by the shear cell, hence different stress directions were applied between the two methods.

We now also consider two additional approaches as outlined in Table 1. As such, uniaxial compression tests and ball indentation measurements onto critically consolidated beds are also carried out. All results shown are for titania (DT51 – Crystal Global).

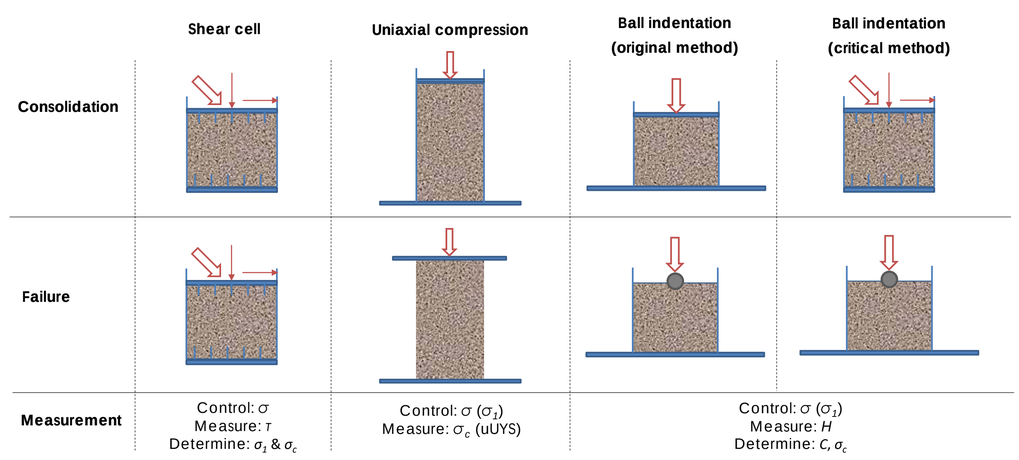

Figure 3. Consolidation and failure modes of applied methods

Table 1. Bed preparation methods applied for indentation and unconfined yield strength measurement

Method	Bed preparation for indentation	Bed preparation for unconfined yield strength	Comments
Mixed (original)	Vertically consolidated	Critically consolidated (shear cell)	• Consolidation and failure stress direction coincident in each test • Stress directions differ between tests
Vertical	Vertically consolidated	Vertically consolidated (uniaxial compression)	• Consolidation and failure stress direction coincident in each test and between tests • Unconfined yield strength underestimated in uniaxial compression
Critical	Critically consolidated (shear cell)	Critically consolidated (shear cell)	• Consolidation stress direction the same in each test • Failure direction differs in indentation • Smooth surface may not be available for indentation

4. Indentation onto a sheared bed

Powder beds were assessed in the FT4 50 mm diameter shear cell at pre-shear normal stresses of 0.5, 1, 2, 3 and 6 kPa, prior to further pre-shearing followed by indentation. Five indents were carried out on each prepared bed (72º separation), with 3 repeats made at each stress (15 indents). Indentations were judged to be reliable if applied to a flat (critically consolidated) surface. At low stresses insufficient powder was retained by the shear head, as such fewer reliable indents were achievable (Table 2).

Table 2. Bed surface available for indentation after critical consolidation

σ	0.5 kPa	1 kPa	2kPa	3 kPa	6 kPa
After lid removal	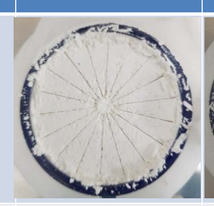				
Reliable indents	0/15	2/15	2/15	4/15	8/15

In an attempt to overcome this problem, beds were sheared using a flat plate of high friction. A flat surface is obtained, however the grip is insufficient to provide adequate shear; leading to a dramatic decrease in the unconfined yield determined by the measurement (Fig. 4). Ball indentation measurements were also made on beds vertically consolidated to the same major principal stress, prepared by first (i) conditioning with the FT4 impeller, or (ii) passing through a 500 µm sieve. The sieve method was applied using both the FT4 and an Instron, hardness measurements are shown in Figure 5 for all methods.

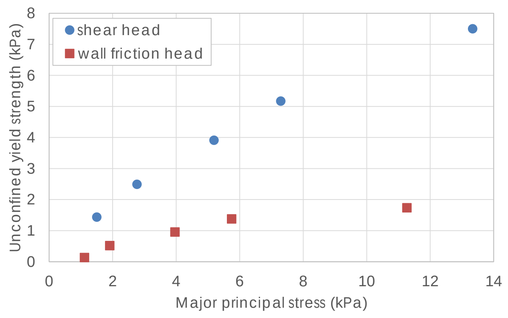

Figure 4. Unconfined yield strength using the standard shear head and a high friction flat plate

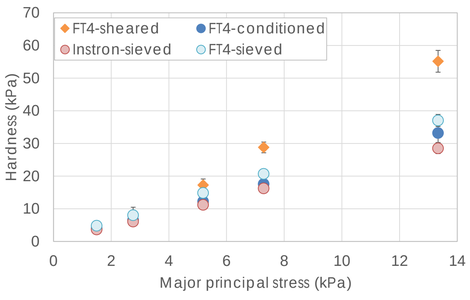

Figure 5. Hardness measurements for vertically and critically consolidated beds

5. Simulation results

DEM simulations of ball indentation allow hardness to be calculated as well as internal bed stresses. The deviatoric stress is calculated using Eq. 4 & 5, and assumed to be representative of the unconfined yield strength, and is assessed inside a measurement cell below the indenter. Figures 9a and 9b show the hardness and deviatoric stress, respectively. Hardness is stable beyond a certain penetration depth, whereas deviatoric stress shows more significant fluctuation around an average value. Constraint factor is determined using Eq. 3 and shown against depth in Figure 10a.

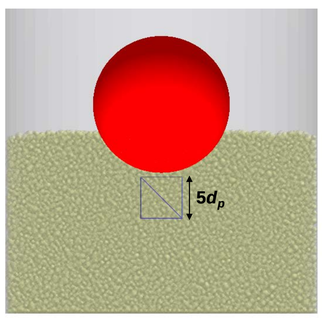

$$\sigma_{ij} = \frac{1}{V}\sum_{1}^{N} F_{ij} \cdot r \quad \textit{(Eq. 4)} \qquad T_D = \frac{\sqrt{(\sigma_1-\sigma_2)^2+(\sigma_1-\sigma_3)^2+(\sigma_2-\sigma_3)^2}}{\sqrt{6}} \quad \textit{(Eq. 5)}$$

The average constraint factor is determined in the dimensionless penetration depth range 0.3 – 0.9. Constraint factor appears to be independent of the consolidation stress (Fig. 10b), though noticeable scatter is observed. The average constraint factor shows a slight increase with sliding (Fig. 11a) and rolling (Fig. 11b) friction coefficients, though this is insignificant compared to the fluctuations observed.

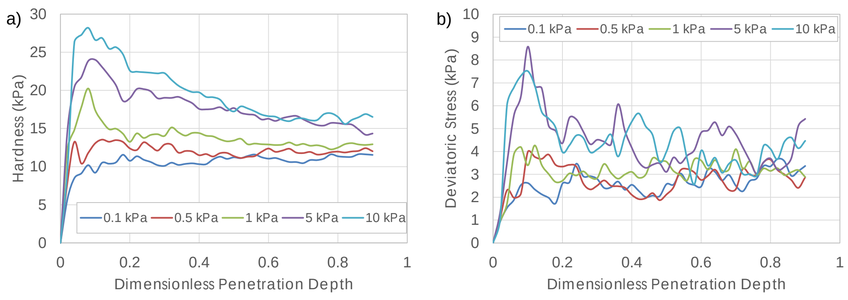

Figure 9. Hardness (a) and deviatoric stress (b) against penetration depth

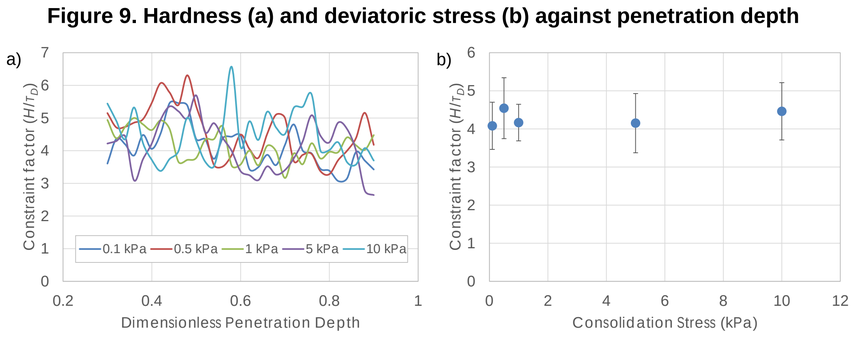

Figure 10. Constraint factor against penetration depth (a) and consolidation stress (b)

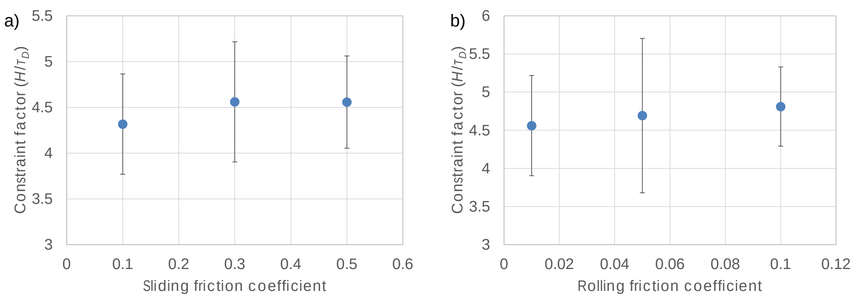

Figure 11. Constraint factor against sliding (a) and rolling (b) friction coefficient

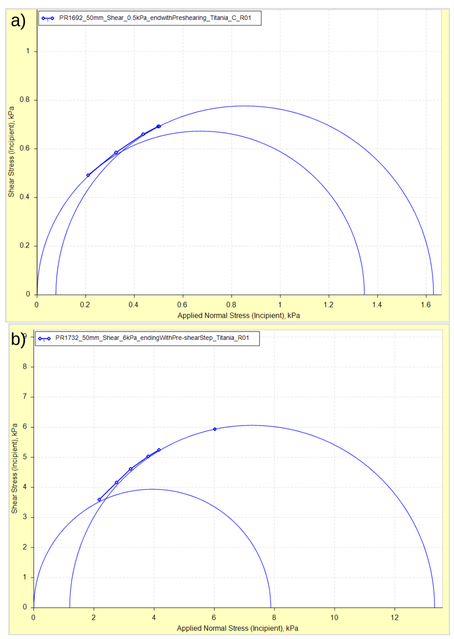

Figure 6. Shear cell measurements at 0.5 (a) and 6 kPa (b) pre-shear normal stress

Figure 6 shows the yield locus determined from shear cell measurements at pre-shear normal stresses of 0.5 and 6 kPa. At 0.5 kPa the mohr circle is tangent to the yield locus, which exhibits slight curvature. In contrast, the yield locus at 6 kPa exhibits significant curvature and the linear fit to the yield locus leads to an overestimate of the unconfined yield strength.

Unconfined yield strength is also assessed using the FT Advanced Uniaxial Powder Tester, and found to be much lower (25-65%) than that measured in the shear cell (Fig. 7).

Figure 8 shows the constraint factor determined by each method outlined in Table 1. With the vertical method *C* is approximately independent of stress, in the range where both methods are reproducible. The mixed method shows an increase in *C* at higher stress, the reason for this is unclear, since previous work showed *C* to be independent of stress with this method. In the critical method *C* is shown to increase significantly with applied stress, perhaps due to the difference in consolidation and failure stress direction in indentation.

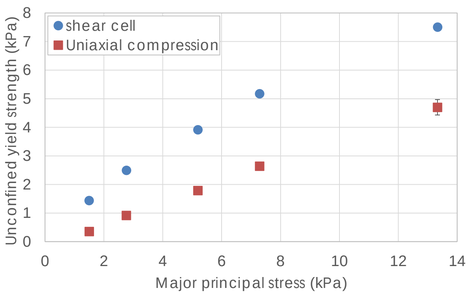

Figure 7. Unconfined yield strength determined by uniaxial compression and shear cell methods

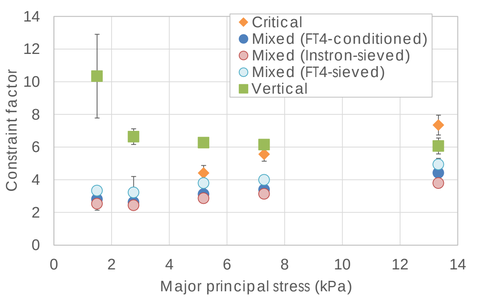

Figure 8. Constraint factor determined by all methods

6. Conclusions and future work

Experimental measurements of titania flowability through the above methods show that:

- Preparation of critically consolidated beds for indentation measurement is challenging, due to insufficient powder being retained in the shear head
- Significant curvature of the yield locus exists, therefore linear approximation leads to inaccuracy in the unconfined yield strength
- Unconfined yield strength measured by the uniaxial compression method is less than that determined in the shear cell, particularly at lower stresses
- Constraint factor determined by the vertical method is almost independent of consolidation stress in the reliable range (> 3 kPa)
- Mixed and vertical methods exhibit an increase in constraint factor with applied stress

DEM simulations of cohesive beads show:

- Constraint factor is independent of applied stress
- Increasing sliding or rolling friction coefficient may increase constraint factor

Though it should be noted that large fluctuations exist

Future work:

- The flowability of various grades of titania will be measured using the approaches applied so far
- In addition the shear cell will be operated under constant volume control, with measurement of normal and shear forces.
- The most promising methods will be applied for other powders, such as alumina, as well as food and pharmaceutical powders.
- A key aspect of the analysis will be to investigate the optimum approach to estimate the curvature of the yield locus.
- The flow field around the ball indenter will be assessed by Synchrotron at the Diamond Light Source (Harwell, UK).

Contact: c.hare@surrey.ac.uk (C. Hare), A.Hassanpour@leeds.ac.uk (A. Hassanpour), a.a.mahmoud@surrey.ac.uk (A. Mahmoud), a.stavrou@surrey.ac.uk (A. Stavrou),

Quantitative Prediction of Segregation at Process Scale

Joseph J. McCarthy

Department of Chemical and Petroleum Engineering University of Pittsburgh, Pittsburgh PA 15261

International Fine Particle Research Institute

ABSTRACT: Segregation rate models hold promise for scale-up via continuum-level analysis using device-specific transport equations. The current focus of our approach involves models that are written expressly in dimensionless form with an aim at transparent scale-up – i.e., inherently scalable segregation rate models. This year has aimed largely at experimental validation of existing segregation rate models. While our scaling approach originally established the first analytical connection between density-based segregation and granular rheology, our recent results not only experimentally support this model, but theoretical efforts have expanded the model to systems that vary by size or shape or applications that have non-trivial degrees of cohesion.

Experimentally Evaluating Models for Segregation

Density Segregation

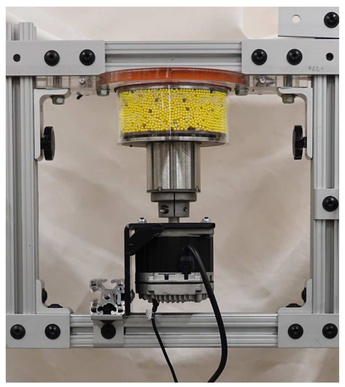

- Experimental apparatus allows constant volume or pressure BC's
- Tracers and a magnet allow high-speed imaging to measure v_s

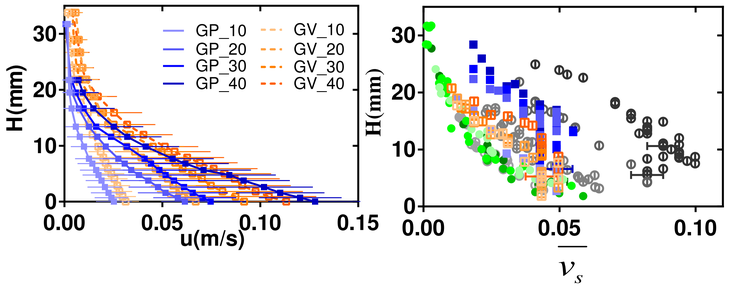

- Inhomogeneous shear means that the inertia number, I, varies with height
- With one experiment we can measure v_s vs I for a range of conditions

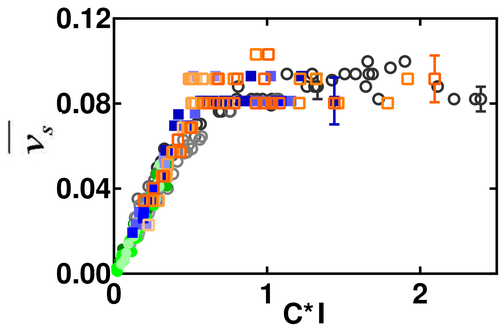

- Results confirm novel segregation saturation model
- Constant, C, required to account for lack of pressure measurement (varies with global shear conditions, but constant within an experiment)

Building New Models for Segregation

Computational Results for Size

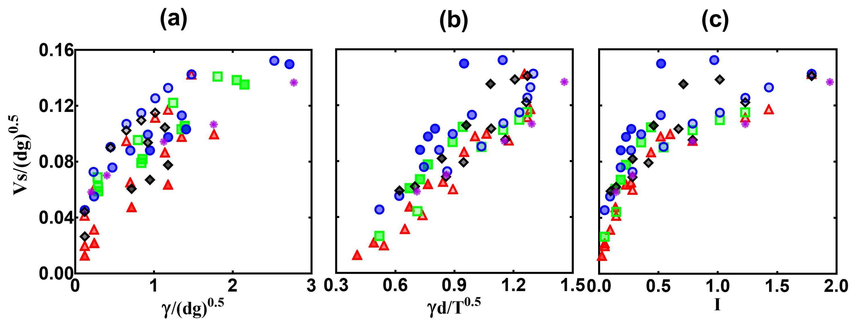

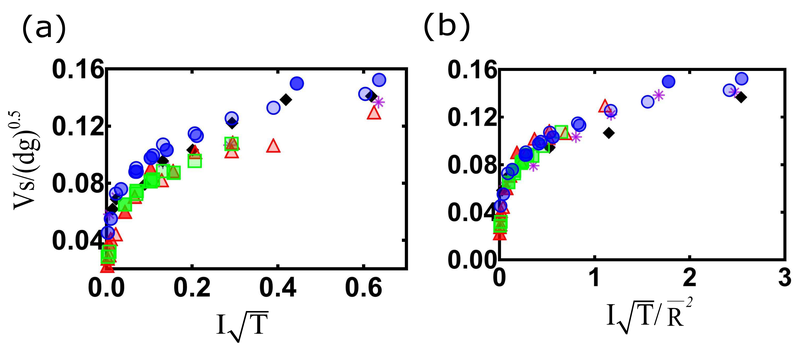

- Size segregation involves a more complex interplay between segregation and rheology
- Simply using the inertia number, I, is insufficient
- Combining I and T captures both creation of voids, as well as exploration of space (finding the holes)
- Novel observation: size ratio scales as the square due to hole size/projected area match

Computational Results for Density-based Cohesion

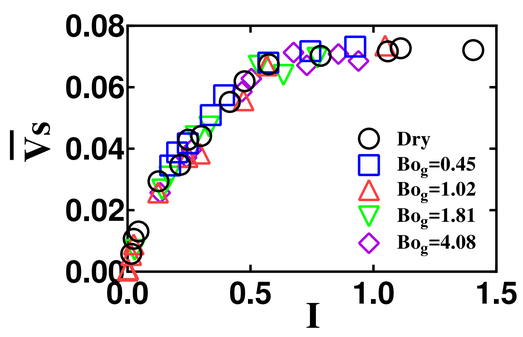

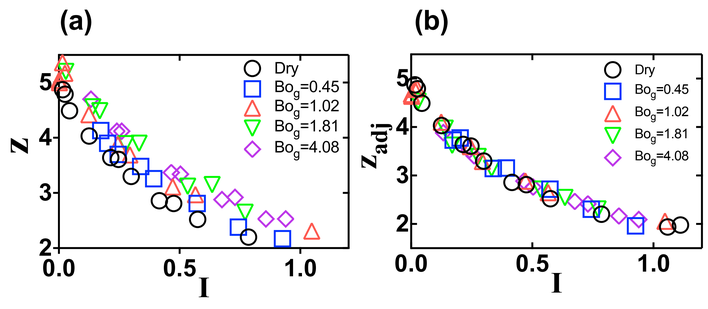

- $\overline{v}_s = \frac{z_{adj}(\bar{p}-1)}{6\beta\sqrt{\bar{p}}} I$ works for **both** cohesive and non-cohesive systems
- $z_{adj} = z \cdot (1 - \frac{F_c}{F_z^t}) = z \cdot (1 - \frac{4\gamma}{\alpha P d_p})$

Experimental Exploration of Shape Segregation

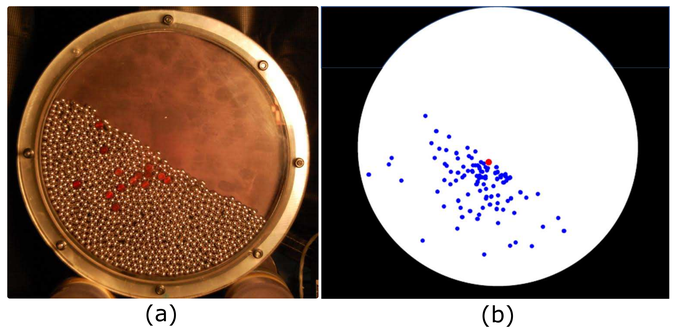

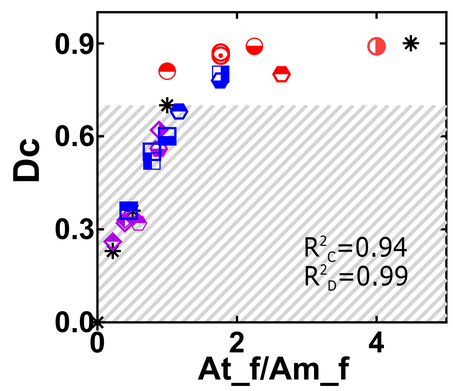

Shape descriptor #	Shortest L	Average L	"Lay down" A	"Spinning" A	Volume	"Flowing" A
Classification #	1D	1D	2D	2D	3D	2D
R^2 Cylinder	0.94	0.79	0.77	0.77	0.65	0.94
R^2 Disc	0.74	0.94	0.99	0.57	0.57	0.99

- Tracking the periodic observed location of tracers allow a measure of segregation based on "distance to center"
- Comparing to sphere-sphere systems allows development of an equivalent shape parameter

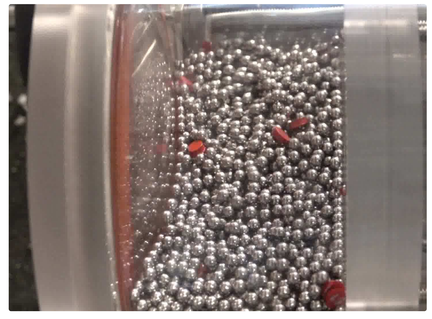

- Note that disks often "roll" down surfaces

Recap and Next Steps on Segregation

- Accomplishments:
  - experimental validation of our novel density-based segregation model
  - extention and computational testing of segregation models based on size differences
  - extention and computational testing of segregation models based on cohesive density-driven systems
  - development of a new model for shape segregation
- Next up:
  - completion of modeling efforts for size, shape, and cohesive segregation
  - additional experimental validation of these models (especially size and cohesion)
  - incorporate our newly developed models into transport equations to enable large-scale validation against process-scale data

A Holistic Approach for the Model-based Control of Crystal Size, Shape and Purity in Integrated Batch and Continuous Crystallization - Wet Milling Systems

Botond Szilagyi, Zoltan K. Nagy

Purdue University, Davidson School of Chemical Engineering, West Lafayette

Specific aims. *"The aim of this project is to develop and provide the first proof-of-concept simulation and experimental demonstration of a real-time implementation of a full population balance model based nonlinear predictive control approach for batch and continuous crystallization processes integrated with wet milling and classification/recycle system, in order to achieve desired crystal size and shape distribution. The effects of impurity/additive mixtures on the size, shape and crystal purity distribution will be incorporated in the model."*

Soft-sensor design

- ***Soft sensor*** based on improved geometrical model
- ***Weighted summing*** of individual crystal's CLDs and ARDs
- ***ANN*** for learning the geometrical model output: efficient memory and ***grid independent***.

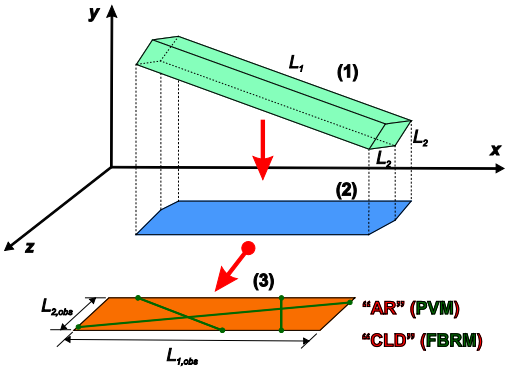

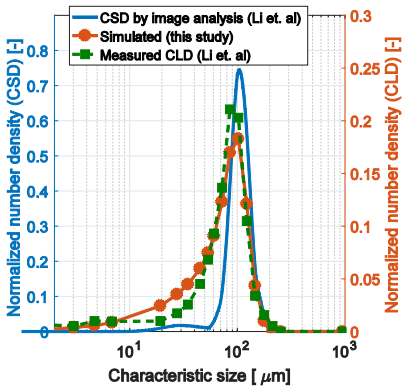

NMPC development

- ***CLD*** as direct feedback information
- ***High fidelity full PBM*** through the ***CrySiV*** function
- ***Kinetic parameter re-estimation*** for adaptive and robust features

CrySiV 2.0

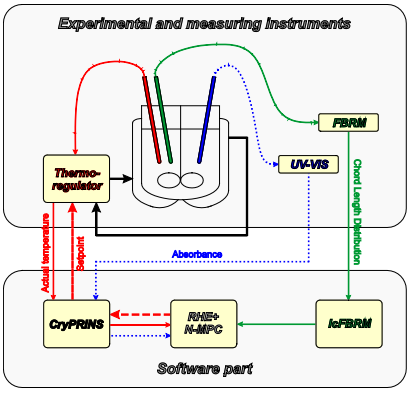

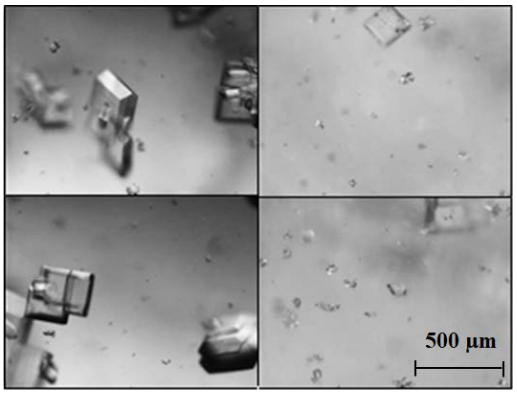

Integrated system

- ***External wet mill*** in external recirculation with batch crystallizer. ***High aspect ratio*** crystals crystallization.
- ***Mechanisms***: nucleation, growth, dissolution. Energy balance, fragmentation and attrition too in the wet-mill.
- ***Better CSD*** with the integrated system. Temperature cycles in the crystallizer

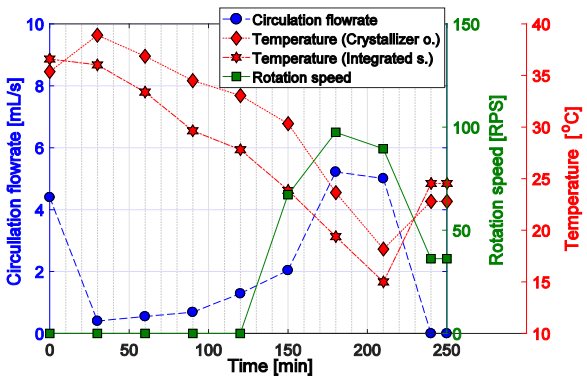

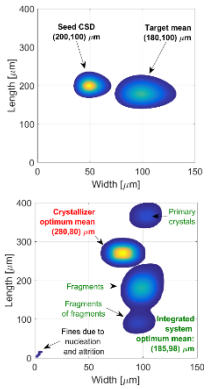

Publications and submitted manuscripts from the last year

[1] Szilagyi, B.; Nagy, Z.K. Population Balance Modeling and Optimization of an Integrated Batch Crystallizer−Wet Mill System for Crystal Size Distribution Control, 2018, Crystal Growth and Design;

[2] Szilagyi, B.; Agachi, P.S.; Nagy, Z.K. Chord Length Distribution Based Modeling and Adaptive Model Predictive Control of Batch Crystallization Processes Using High Fidelity Full Population Balance Models, 2018, Industrial and Engineering Chemistry Research;

[3] Szilagyi, B.; Nagy, Z. K. Aspect ratio distribution and chord length distribution driven modeling of crystallization of two dimensional crystals for real-time model based applications, Crystal Growth and Design, submitted

[4] Szilagyi, B.; Borsos, A.; Pal, K.; Nagy, Z. K. Experimental implementation of a mechanistic PBM-based nonlinear model predictive control involving chord length distribution measurement for the batch cooling crystallization of L-ascorbic acid, Chemical Engineering Science, submitted

Milling and Material Grindability
modelling, measurement and mill fingerprinting

J.Y. Ooi, X.Z. Chen, L.G. Wang, J.F. Chen** and J. Sun*

Institute for Infrastructure and Environment, School of Engineering, University of Edinburgh, Scotland, UK

*Department of Chemical and Biological Engineering, University of Sheffield, England, UK

**School of Planning, Architecture and Civil Engineering, Queen's University Belfast, UK

1. Project overview

The goal is to develop a generic methodology to link material grindability with particle dynamics in a mill.

Main objectives include:

- Understanding the local stressing events
- Characterising the comminution behaviour
- Establishing dominant fragmentation mechanisms
- Validating through milling experiments

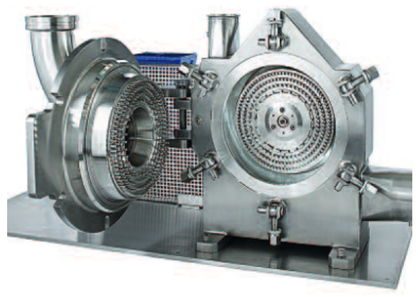

Impact pin mill

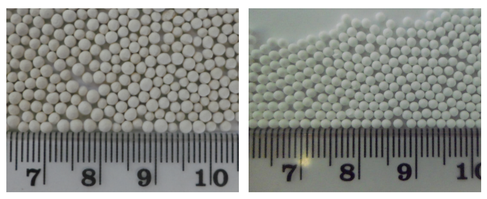

Synthetic zeolite (left) and alumina (right)

2. Understanding grindability

---What are the experimental and numerical methodologies?

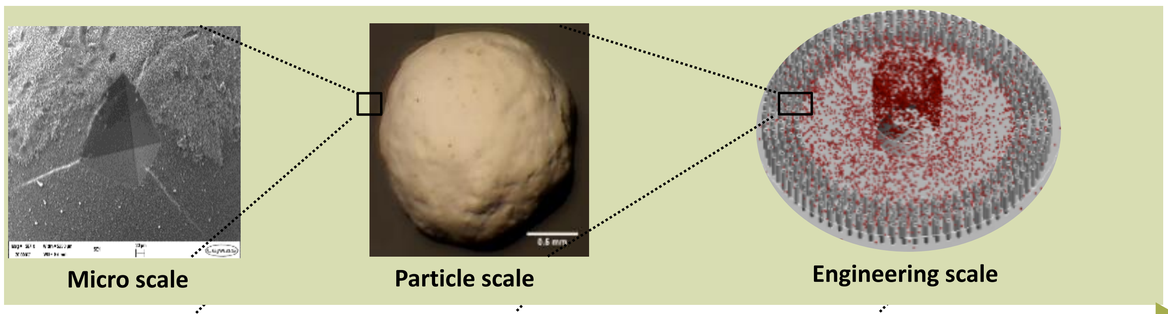

$$\varepsilon \propto \frac{\rho^{1/4} R^2 H^{1/2}}{k_c^{5/2}} v^{9/2}$$

kc: Fracture toughness
H: Particle hardness

$$\sigma_{T,\max} = \max\left[0,\ \max\left(\frac{F_{ix}}{A_B} \pm \frac{R_B\sqrt{M_{iy}^2 + M_{iz}^2}}{I_B}\right)\right] \quad i = \alpha, \beta$$

Forces and torques calculation based on Timoshenko beam theory

$$m_a \frac{d\mathbf{u}_a}{dt} = \mathbf{F}_{contact,a} + \mathbf{F}_{ext,a}$$

$$\frac{d\mathbf{r}_a}{dt} = \mathbf{u}_a \quad \mathbf{I}_a \frac{d\omega_a}{dt} = \mathbf{T}_a$$

$$\frac{\partial M_p(x,t)}{\partial t} = -S_M(x) M_p(x,t) + \int_0^\infty S_M(y) M_p(y,t) b_M(x,y)\, dy$$

$$S_M(x) = Sc_M\left[1 - \exp\left(-f_{mat} x \left(W_{m,kin} - W_{m,\min}\right)\right)\right]$$

$$B_M(x,y) = \frac{1}{2} \cdot \left(\frac{x}{y}\right)^q \cdot \left(1 + \tanh\left(\frac{x - x'}{x'}\right)\right)$$

➢ **DEM-PBM Upscaling strategy to predict grindability**

3. Theoretical model development

--- capturing the effect of impact angle on particle breakage

- Assumption: lateral crack is responsible for chipping mechanism; Normal impact breakage model was proposed based on indentation fracture mechanism
- Previous models **only considered** the normal component of the impact velocity: the tangential component is **ignored**
- Experimental evidence shows the **significance of tangential component** (Figure in right hand)
- The effect of the incidence angle may be considered using the following equivalent velocity:

$$v_{eq} = \sqrt{(sin^2\theta + \alpha^2 \mu^2 sin^2\theta cos^2\theta)}\, v$$

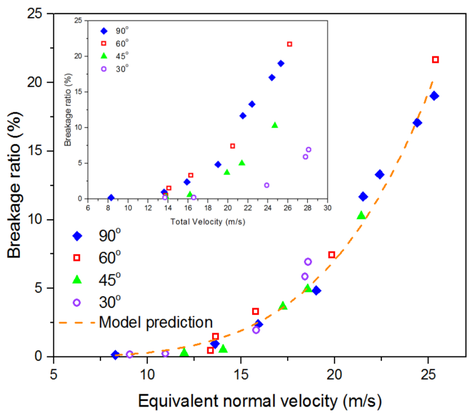

Zeolite impact test

➢ Breakage ratio increases dramatically over 15 m/s and increases with increasing impact angle (90° is normal impact)

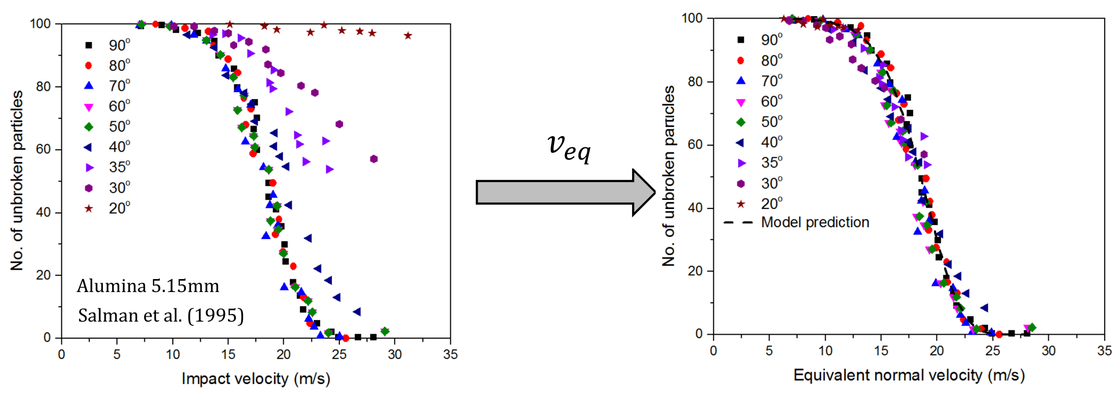

➢ The equivalent normal velocity proposed successfully predicts the breakage under various oblique impacts for both chipping and fragmentation

4. Bond DEM simulation

---How will particle break under high impact velocity?

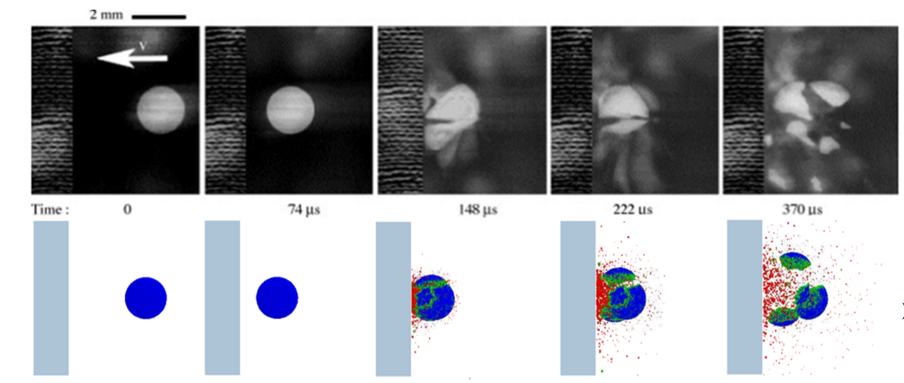

➢ **Tension failure dominant**

➢ **Comparison between the bonded DEM model and the experiments of Antonyuk *et al* 2006 (*23* m/s)**

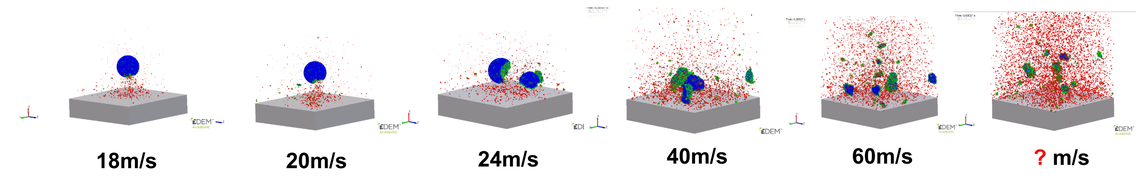

➢ **Breakage under increasing impact velocities as predicted using DEM bond particle model**

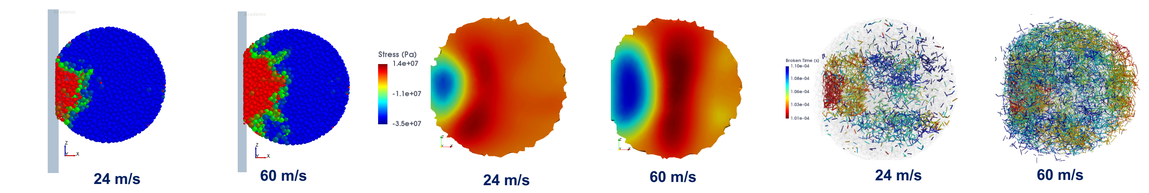

➢ **Higher impact velocity generates a stronger tensile zone leading to more drastic damages**

5. Mill function

-- What are the key particle dynamics in a mill?

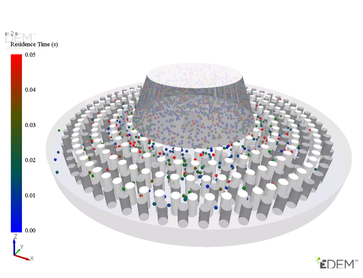

DEM simulation of UPZ100 mill

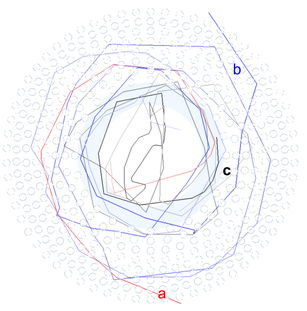

Trajectories of particles

Impact statistics

Average variables/RPM	8000	10000	12000	18000
Residence time (ms)	86	71	61	44
Impact per particle (-)	175	179	184	183
Impact velocity (m/s)	46	58	70	104
Normal velocity (m/s)	33	42	49	73
Tang. velocity (m/s)	27	34	40	61
Normal force (N)	36	47	58	93
Tang. Force (N)	4	6	7	12

➢ **DEM simulations were performed to obtain the particle dynamics and stress event statistics**

➢ **Average impact velocity in pin mill is high and oblique impacts prevail**

6. Milling prediction

--- How to link material and mill function to make a reliable prediction?

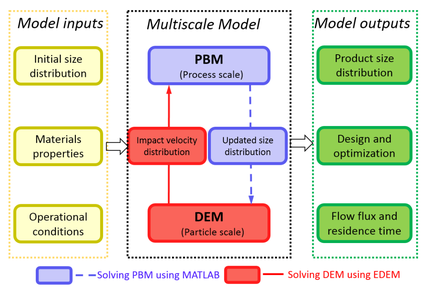

DEM-PBM multiscale coupling

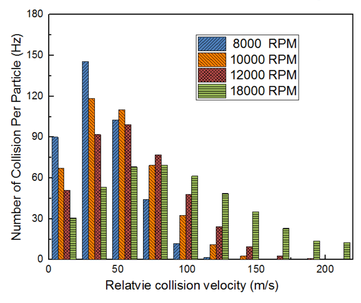

DEM: Impact velocity distribution

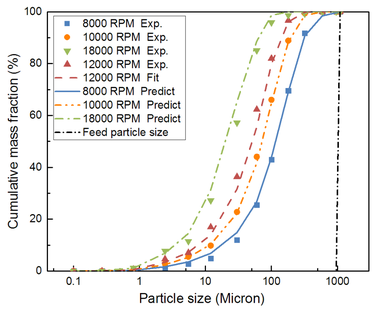

PBM: product size distribution

➢ **Impact velocity distributions from DEM were used to inform the PBM kernels quantitatively.**

➢ **One milling test data are used to calibrate the material parameters**

➢ **DEM-PBM coupling prediction show good agreement with the milling experimental results**

7. Summary remarks

--- Lessons learned and further work

- Static, indentation and impact loading tests were deployed to characterise particle properties
- New model for impact loading breakage was proposed to include the effect of impact angle
- Bond particle model was used to extend the predictions for high velocity impact breakage
- DEM was used to obtain the dominant stress events inside pin mill for various conditions
- DEM-PBM multiscale coupling was developed to predict the milling products of the pin mill
- Further work on the refinement and extension to other processes are ongoing

Acknowledgements

- Hosokawa Micron Ltd., UK
- Process System Enterprise, UK
- DEM Solutions Ltd, Edinburgh, UK; Leeds University, UK
- The International Fine Particle Research Institute, IFPRI

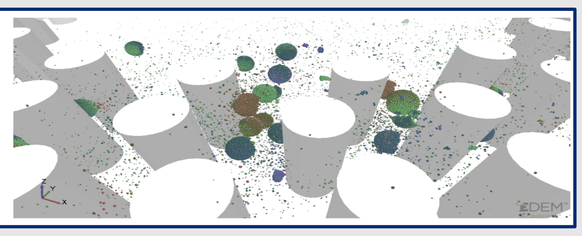

TECHNISCHE UNIVERSITÄT BERGAKADEMIE FREIBERG
The University of Resources. Since 1765.

INSTITUTE OF MECHANICAL PROCESS ENGINEERING AND MINERAL PROCESSING

DETAILED INSIGHT INTO MICROSCOPIC FILTER CAKE PHENOMENA USING 3D-TOMOGRAPHY

M. Mohammadfoghi, E. Löwer, T. Leißner, U.A. Peuker

SUPPORTED BY IFPRI International Fine Particle Research Institute

PARTICLE PROPERTIES
- particle shape
- particle size
- particle-particle interaction

FILTER CAKE PROPERTIES
- integral porosity
- pore size
- trapped liquid areas

PROCESS RELEVANT PROPERTIES
- dewatering behavior
- moisture content
- specific cake resistance

MEASUREMENT PRINCIPLE

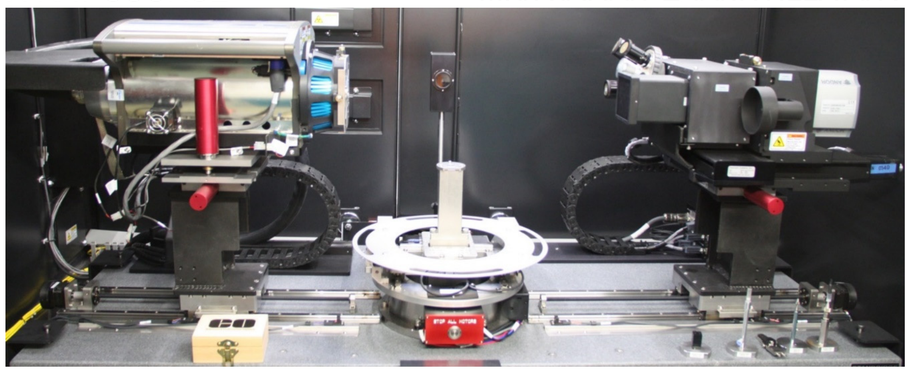


FLOW-CELL

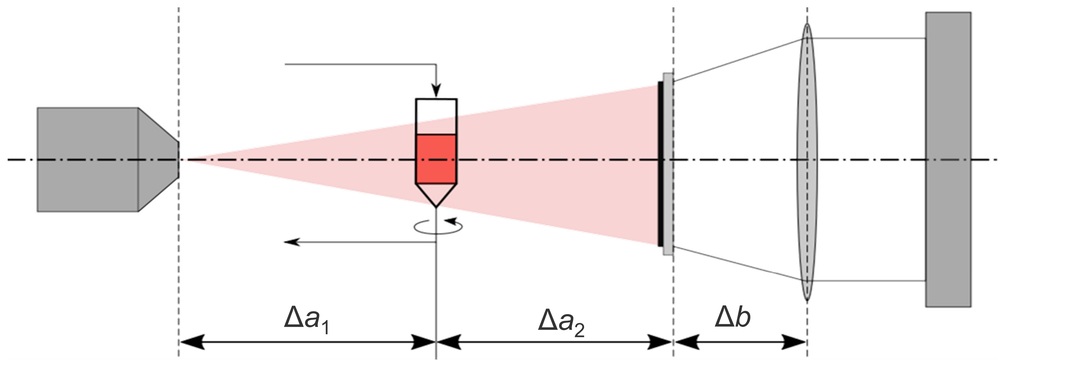

X-ray source	sample/flow-cell	scintillator and optics	CCD-camera
voltage/power: 20-160 kV/1-10 W	**Sample size**: 5 x 5 x *h* mm³	**magnificiation:** $\frac{\Delta a_1 \Delta a_2}{\Delta a_1} \Delta b$	**Voxel size:** (0.7-5 µm)³

IN-SITU MEASURING SET-UP

DOWN-SCALE: $A_{\mathrm{VDI}}/A_{\mathrm{insitu}} = 100$

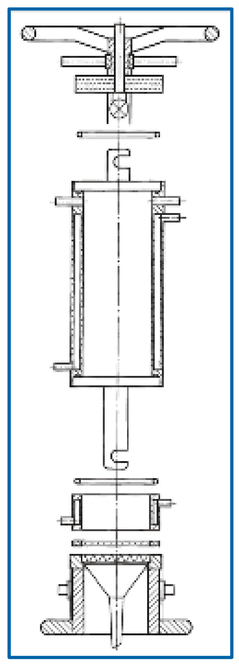
VDI 2762
⌀ 50 mm

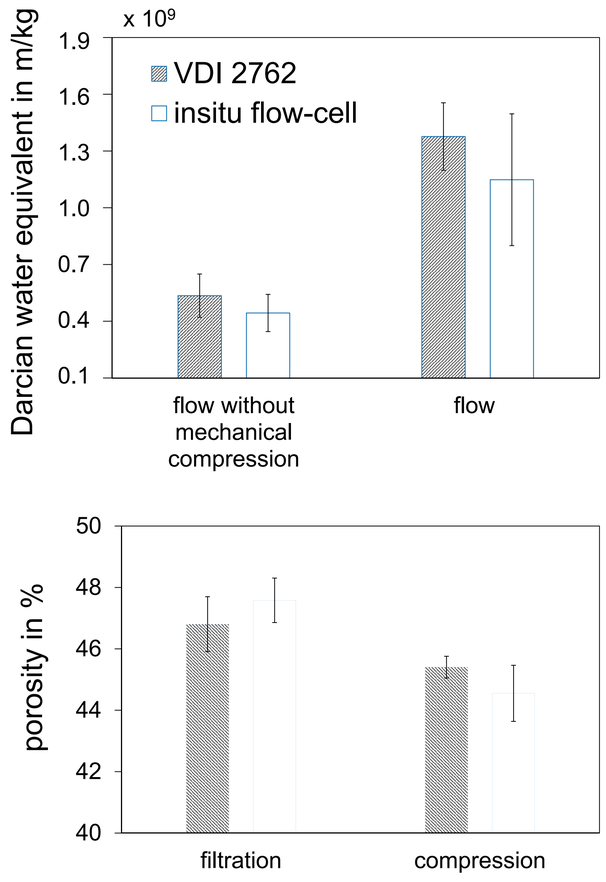


insitu flow-cell
⌀ 5 mm

SCOPE OF THE PROJECT

compact particles

crushed Al_2O_3

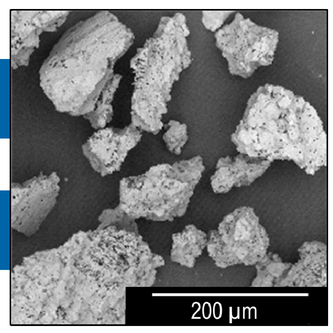

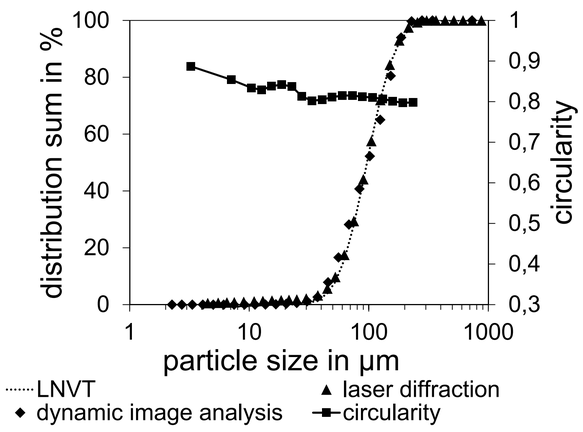

COATING/ SILANISATION

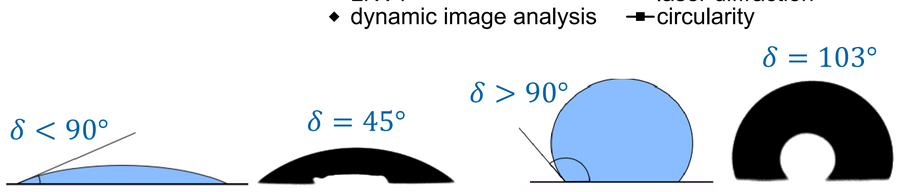

needle-like particles

wollastonite $CaSiO_3$

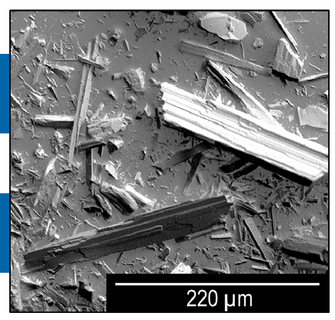

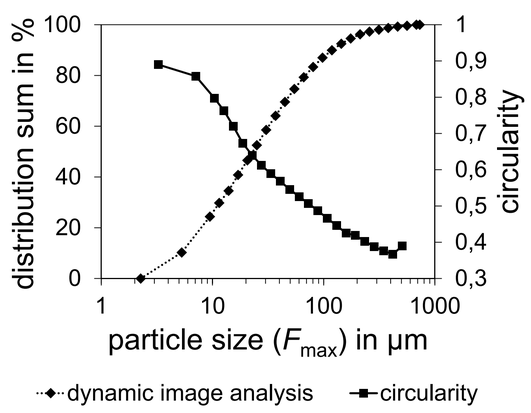

RESULTS

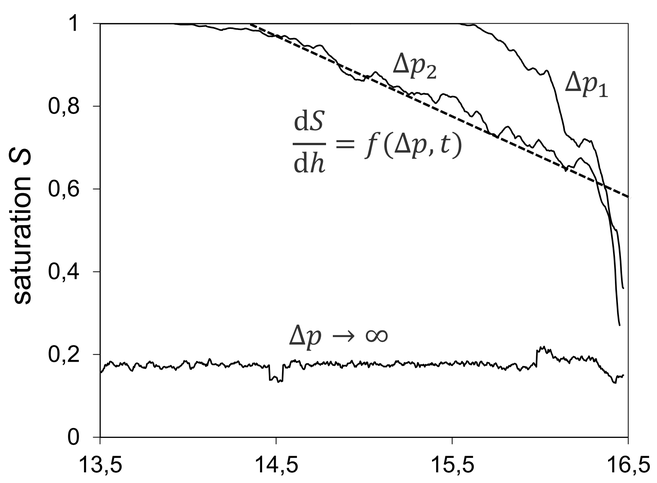

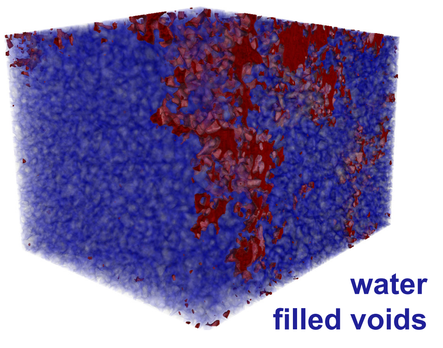

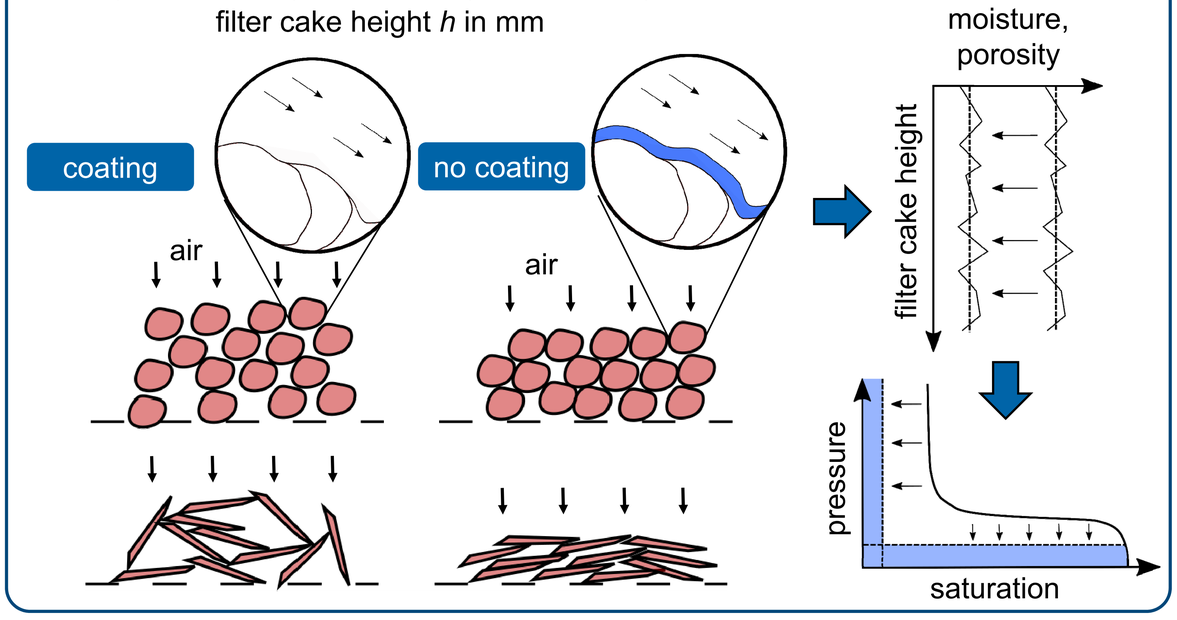

Prof. Dr. Ing. U. A. Peuker
TU Bergakademie Freiberg | Institute of Mechanical Process Engineering and Mineral Processing | Agricolastraße 1 | 09599 Freiberg/Germany | +49 3731 39-2916 | Urs.Peuker@mvtat.tu-freiberg.de |
IFPRI annual meeting Edinborough | June 2018

The Stability of Colloidal Gels to Gravity and External Shear

Xuemao Zhou, Joost de Graaf, Michiel Hermes, Yujie Jiang, John Royer, Wilson Poon

School of Physics and Astronomy, The University of Edinburgh, Edinburgh, United Kingdom

w.poon@ed.ac.uk

EPSRC Engineering and Physical Sciences Research Council

MARIE CURIE ACTIONS

Schlumberger

CHINA SCHOLARSHIP COUNCIL

IFPRI

We have previously discovered a key role of the air-gel meniscus in causing gravitational collapse. Now, using a bespoke apparatus, we have discovered exactly how the meniscus plays this role: *any* curvature of *either sign* gives rise to unbalanced tangential forces destroying gel structure and forming debris that falls and initiates collapse. We are also able to simulate gel formation under gravity with full hydrodynamics. We discovered that below $\phi \approx 0.1$, where there is no pre-existing percolating cluster, hydrodynamics cause an accelerating interface. The effect is absent for $\phi > 0.1$ and for all ϕ without hydrodynamics. Finally, we have started experiments using a model binary system of large hard particles suspended in a background matrix of a small-particle gel. We discovered that the presence of the large particles fundamentally alters the rejuvenation dynamics of the background gel matrix.

Summary of Gravitational Collapse Experiments on Monodisperse Gels

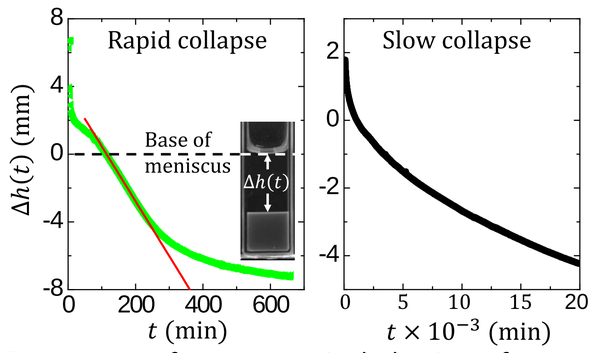

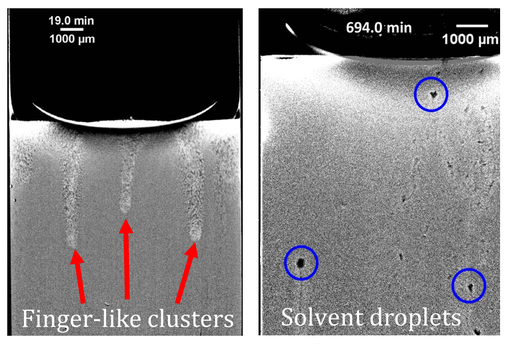

Two types of macroscopic behavior of an experimental model system of $d{\sim}2\ \mu\text{m}$ PMMA colloids + polystyrene in a solvent mixture of cis-decalin and tetralin. **(left)** The position of the gel interface with respect to the meniscus, Δh, is plotted against time t. **(right)** Optical microscopy images of falling finger-like clusters and rising "pure" solvent droplets; compare [1].

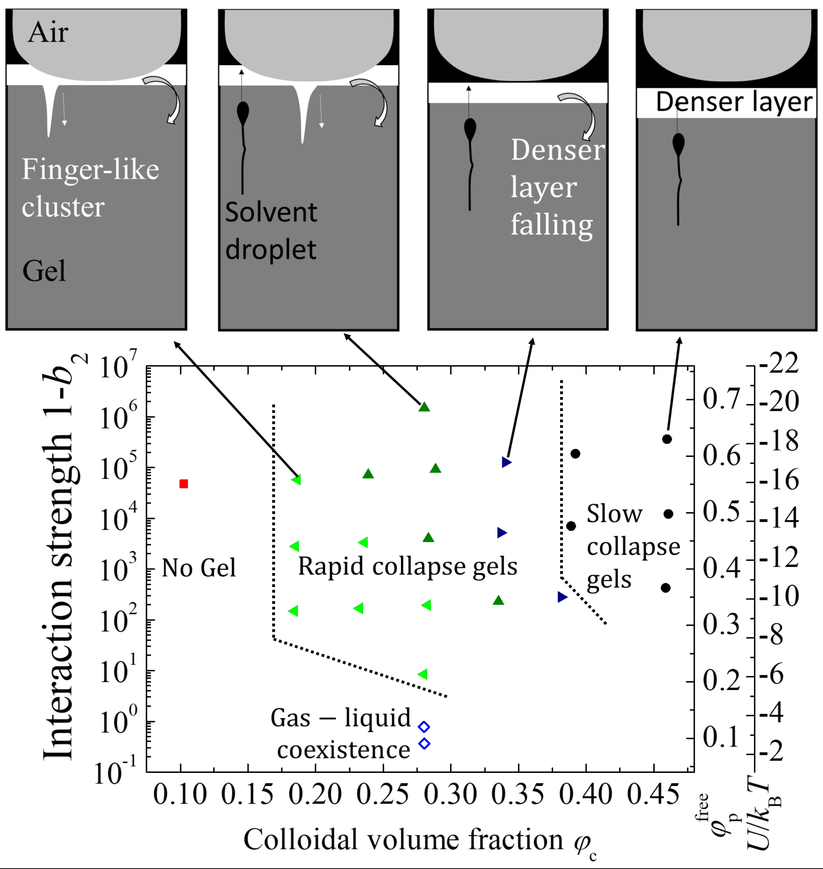

Sketches of the four collapse mechanisms.

The state diagram of [2] refined by adding the different collapse regimes.

Probing the Effect of Meniscus Curvature on the Gravitational Collapse

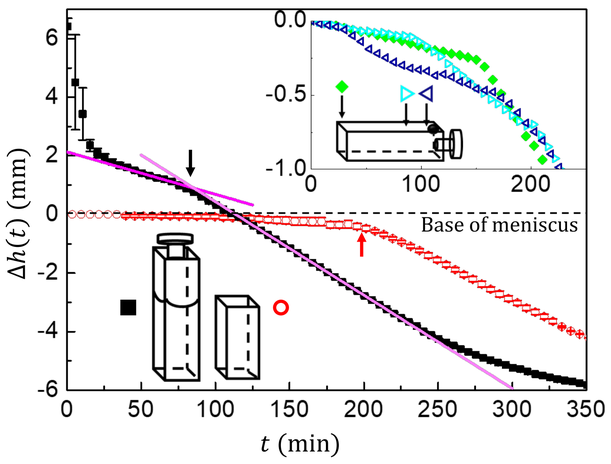

← Collapse can be postponed by removing the curved meniscus.

(left) Varying the curvature of gel meniscus by controlled filling. **(mid-top)** Side view. **(mid-bottom)** PIV velocity map of top view. **(right)** Force balance on a particle at a concave meniscus. The weight component ⊥ the interface is balanced by depletion attraction, but an unbalanced ∥ component remains. ↓

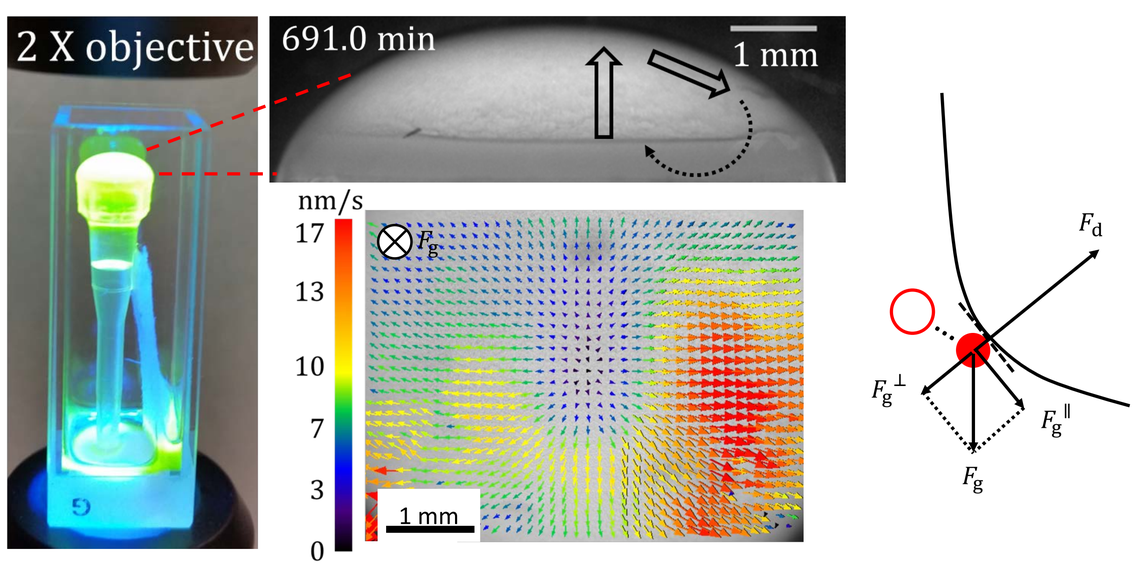

Hydrodynamic Simulations of Gel Collapse

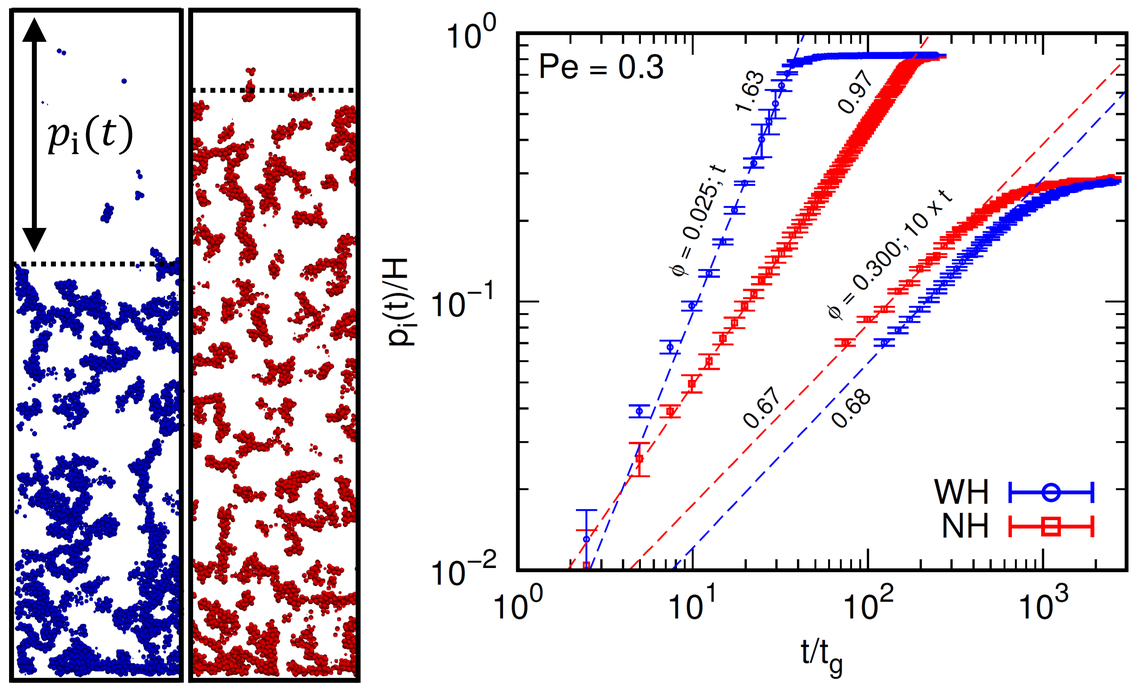

(left) Snapshots showing a slice of a collapsing gel at equal time for a system with fluid flow (blue; WH) and without (red; NH). **(right)** The height $p_i(t)$ of the gel-free zone, divided by the total height H, as a function of time t, divided by the sedimentation time t_g.

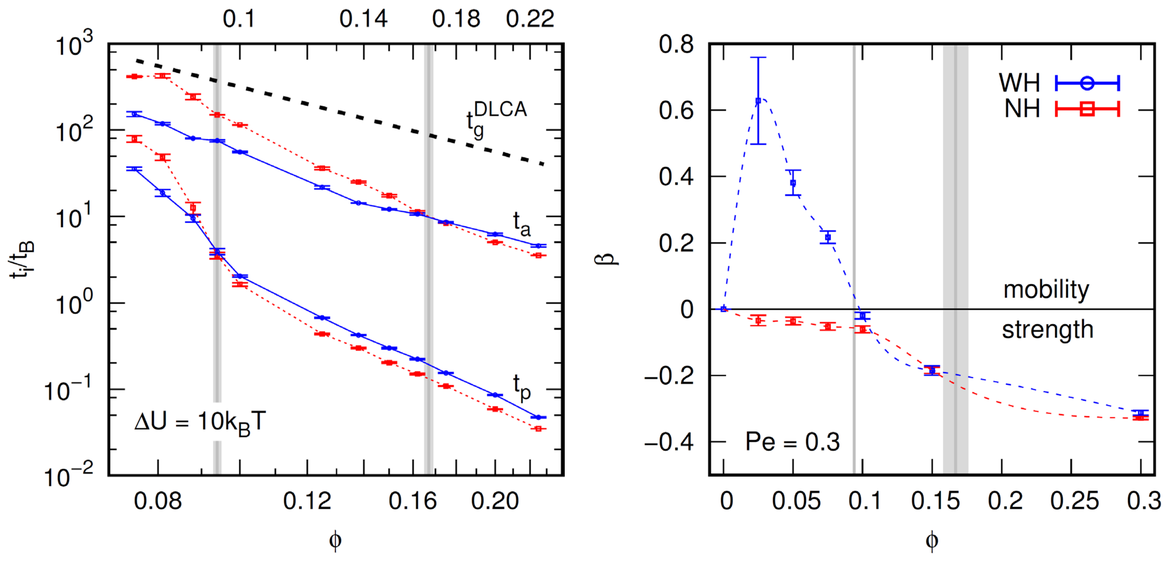

(left) The time to percolate in bulk t_p and for aging to set in t_a, divided by the Brownian time t_B, as a function the colloid volume fraction ϕ, for a *bulk* gel system *without* gravity. The two gray lines indicate a crossover between systems with and without hydrodynamic interactions. The dashed line indicates the DLCA gelation prediction. **(right)** The exponent β of the interface-velocity power law of gravitational gel collapse $v = dp_i/dt \propto t^{\beta}$.

Steady Shear Experiments on Bi-Component Gels:

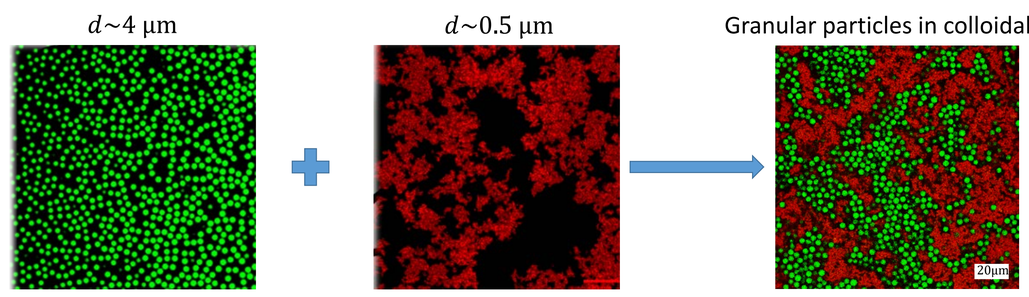

Large *hydrophilic* silica colloids that are stable in water are mixed with small *hydrophobic* silica colloids that gel. When combined in water/glycerol, we obtain a model system where large repulsive particles are embedded in a colloidal gel of attractive small particles.

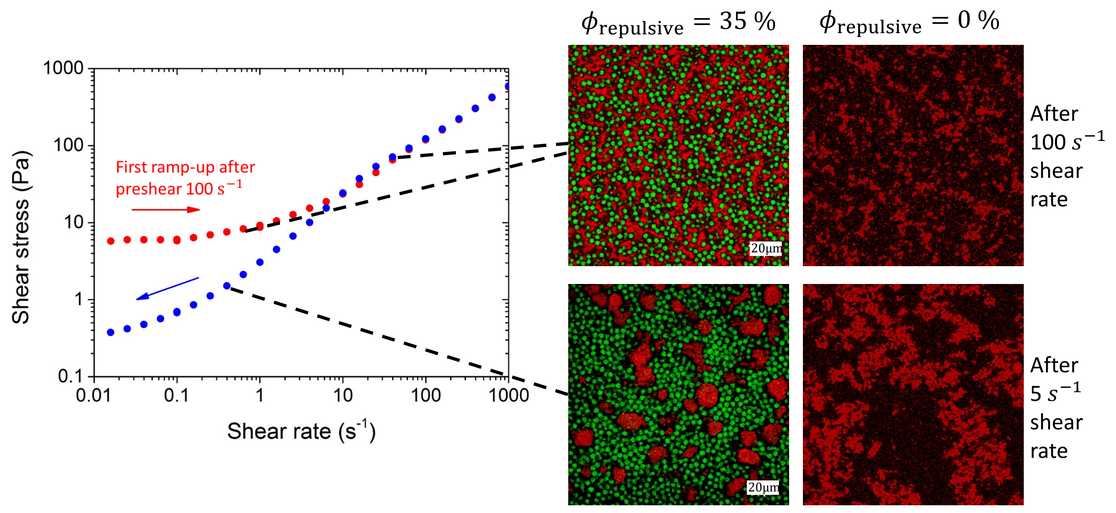

After high pre-shear the colloidal gel breaks up and disperses among the large particles to rejuvenate a gel matrix. However, moderate shear causes the gel to phase separate into compact, disjoint clusters. This effect results from the presence of the large particles, since no such structural change is observed in the pure gel (for which see [3] for details).

This work is funded by IFPRI, EPSRC, CSC, Schlumberger and the EU.

[1] L. Starrs, W.C.K. Poon, D.J. Hibberd, M.M. Robins: "*Collapse of transient gels in colloid-polymer mixtures*." J. Phys.: Cond. Mat. **14**, 2485 (2002).

[2] R. Harich, T.W. Blythe, M. Hermes, E. Zaccarelli, A.J. Sederman, L.F. Gladden, and W.C.K. Poon: "*Gravitational collapse of depletion-induced colloidal gels*." Soft Matter **12**, 4300 (2016).

[3] N. Koumakis et al., "*Tuning colloidal gels by shear*", Soft Matter **11**, 4640 (2015).

Self-Assembled Monolayers as Nucleating Surfaces to Study Early Formation Pathways of Crystal Polymorphs

Jiazhen Xu[1], Ethan M. Susca[1], Detlef M. Smilgies[2], Lara A. Estroff[1], Ulrich B. Wiesner[1]

[1]Department of Materials Science and Engineering, [2]Cornell High Energy Synchrotron Source, Cornell University, Ithaca, 14853

Motivations:

- Polymorphism refers to crystalline solids with different arrangements of same constituents
- Polymorphs affect properties including processing or bioactivity, *e.g.* of products in the pharmaceutical industry
- Previous years: Different surface chemistries of self-assembled monolayers (SAMs) with various solvents enabled polymorph selection for acetaminophen (ACM)

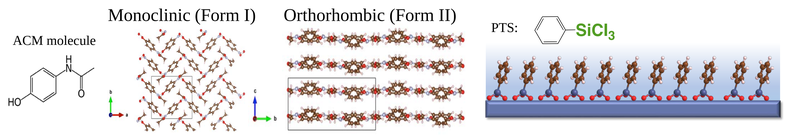

- Phenyltrichloro-silane (PTS) based SAMs on silicon wafer provide pathways to forms I & II of ACM
- Now: Study of early ACM crystal formation stages using in-situ synchrotron based wide-angle x-ray scattering

Spontaneous nucleation & growth of form II:

- 10μL of ACM in water/dioxane droplet on PTS at 50°C
- Water/dioxane solution is a reliable precursor for form II
- Sample is first characterized by general area detector X-ray diffraction system (GADDS)
  - Highly viscous solution lasts long time before (002) peak occurs first, followed by other peaks

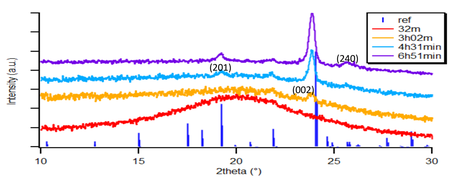

Growth of form II by seeded nucleation:

- 200μL of concentrated ACM in water/dioxane solution was deposited on PTS at 50°C in 10μL increments creating long and narrow continuous 'thin – films'

- 1-2: Solvent evaporation concentrates solution
- 3: Add additional solution to make larger droplets
- 3-4: Repeat 1 & 2 multiple times
- 4: Connect solution droplets to form large single droplet
- 5: Continue to add solution to create a long narrow shape

- Water/dioxane solvent mixture upon evaporation forms an amorphous 'long-lived glassy' solution
- Add form II seed crystal to one end of elongated solution to initiate crystallization and determine growth direction
- Optical micrographs show the growth front revealing a slightly curved dark line running ahead of 'main crystal'

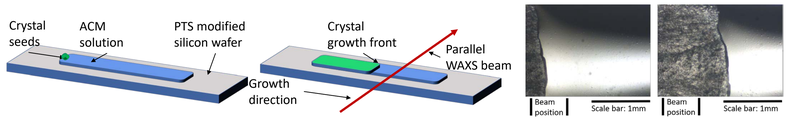

- Use *in-situ* synchrotron based WAXS at Cornell High Energy Synchrotron Source (CHESS) to probe different vertical film positions: middle and bottom

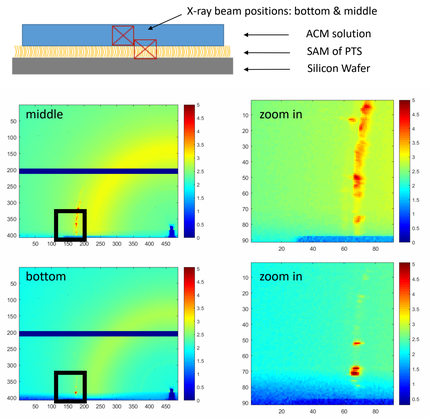

- In-plane (002) is first peak occurring in 2-D WAXS patterns
- Frames shown are 8s after first crystal occurs
- Wider azimuthal spread of 'middle' signal suggests crystals grow up from substrate – solution interfaces

- Final 'thin-film' morphology from scanning electron microscopy (SEM) at 300V
- Central branches are parallel to growth direction
- Secondary branches spread off parallel with twinning-like boundaries between central branches
- Voids are formed near central branches indicating inhibition of growth

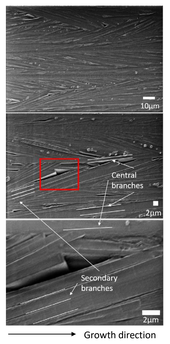

Spontaneous nucleation & growth of form I:

- 10μL of ACM water droplet on PTS at 50°C

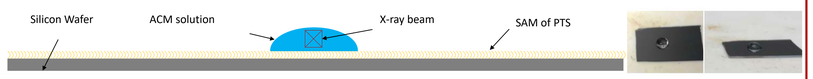

- Use *in-situ* synchrotron based WAXS at CHESS to record spontaneous nucleation and growth events of form I

- Spontaneous nucleation at a position within beam path is a 'rare event'
- Faceted nucleation in optical micrograph suggests initial growth of single crystal
- High time resolution (10 frames /s) allows to distinguish the very first occurring peak

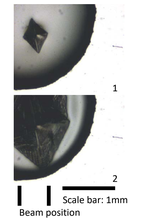

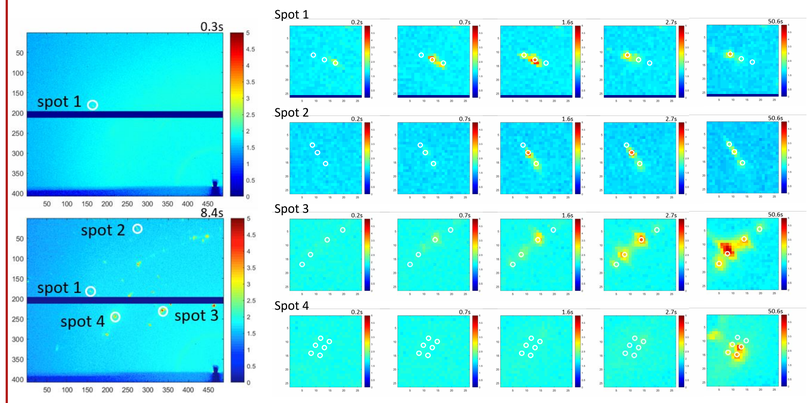

- Identify the first spot in WAXS pattern
- Time evolution of the first spot shows a shift along scattering vector, q, direction between 3 positions
- Comparison with other 'early stage' spots reveals that other spots don't show same shift along q, but rather changes in intensity along q or in azimuthal positions

Conclusions:

- *In situ* synchrotron work provided first insights into early ACM crystal formation stages
- Studies of ACM form II on PTS SAMs in dioxane/water revealed growth upwards from substrate-solution interface
- Studies of spontaneous nucleation of ACM form I on PTS SAMs in water revealed unusual peak shifts at the earliest time points hinting at possible early structural transformations (versus simple rotations).
- These results warrant further in-depth studies of these early formation stages

Future directions:

- Continuing with *in situ* GIWAXS performed at CHESS
- Introducing blade coating as an alternative method
- Introducing other model systems: e.g. 5-methyl-2-[(2-nitrophenyl)amino]-3-thiophenecarbonitrile (ROY)

Gravity and Suction Filling of Pharmaceutical Powders

International Fine Particle Research Institute

Anastasiya Zakhvatayeva, Colin Hare and Chuan-Yu (Charley) Wu

Department of Chemical and Process Engineering, University of Surrey, Guildford, GU2 7XH, U.K.

C.Y.Wu@surrey.ac.uk

1. Introduction

Die filling is a critical process step in pharmaceutical tablet manufacturing. Mass and content uniformity of the tablets as well as the final production throughput depend upon the die filling performance of pharmaceutical formulations.

It is therefore important to understand how powder characteristics and die filling systems influence the efficiency of die filling.

2. Materials

The study was performed using seven excipients commonly used in the manufacturing of solid oral dosage forms.

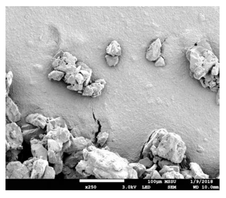

Lactose monohydrate

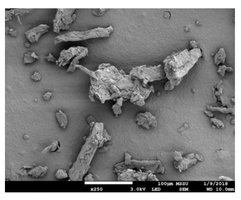

MCC DG

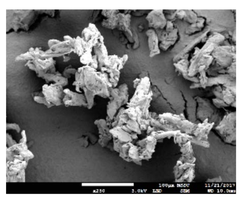

MCC PH101

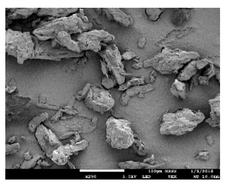

MCC PH102

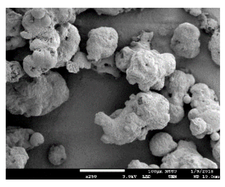

Mannitol

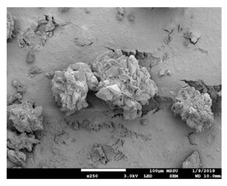

Dicalcium phosphate anhydrous

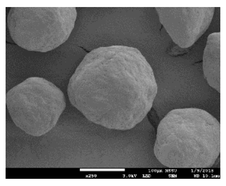

MCC CP102

3. Experimental set up

The die filling behaviour of the powders was explored using two types of die filling systems:

a)Linear die filling system (Fig.1), consisting of:

- moving feeder(*fill shoe*),

- stationary die.

b) Rotary die filling system (Fig.2), consisting of:

- stationary fill shoe,

- moving die (Fig.3).

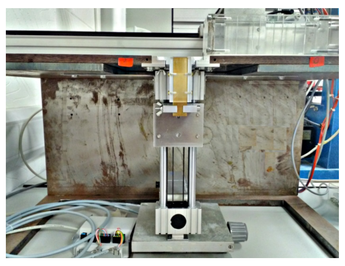

Fig.1

Fig.2

The linear die filling system is also equipped with a vertical displacement drive, connected to a piston (Fig.4). This configuration is used to investigate the suction filling mechanism.

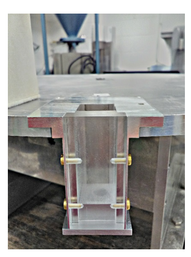

Fig.3

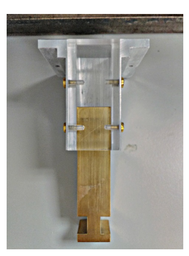

Fig.4

3. Powder characterization

The following powder properties were investigated:

- Morphology (SEM)
- Mass flow rate (Flodex)
- Particle size distribution (Sympatec)
- Specific Energy (FT4)
- Air permeability (FT4)
- Cohesion and flow function (FT4).

The variation of the fill ratio with the fill speed was analysed for the two devices. The suction filling was further investigated for Lactose, MCC PH102 and MCC CP102 on the linear device.

4. Results

Linear die filling vs rotary die filling

Linear die filling

The top sequence is typical of cohesive powders (intermittent flow) like Lactose monohydrate (average particle size 50 micron), MCC DG and MCC PH101.

The sequence in the middle describes a more freely flowing MCC PH102.

The bottom sequence is typical of less cohesive, free flowing DCPA, Mannitol and MCC CP102.

Rotary die filling

The flow profiles are similar to those observed on the linear system , but the efficiency of die filling is on average higher (see graphs below).

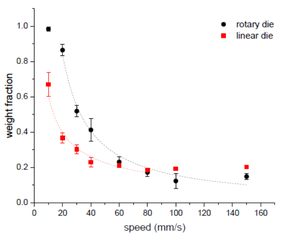

Lactose monohydrate

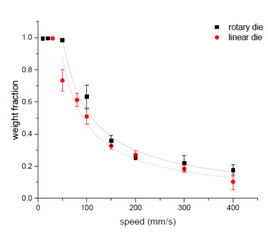

MCC PH102

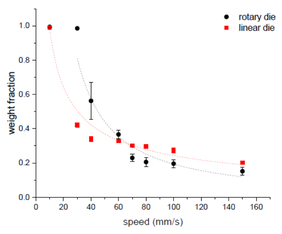

MCC DG

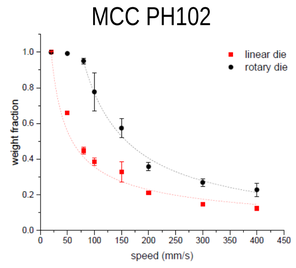

Mannitol

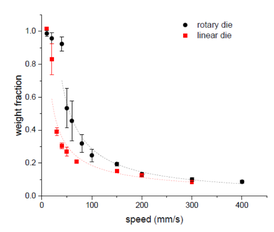

MCC PH101

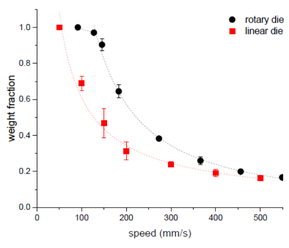

DCPA

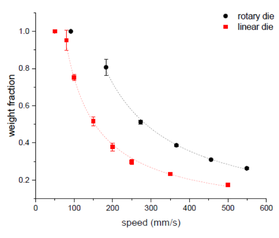

MCC CP102

The rotary die filling system performs better than the linear one:

- At low values of fill speed, the fill ratio tends to be high for both the systems.
- As the speed increases the difference between the linear and the rotary devices in terms of fill ratio becomes more evident for free flowing powders (See mannitol, DCPA and MCC CP102).

Gravity die filling vs suction filling

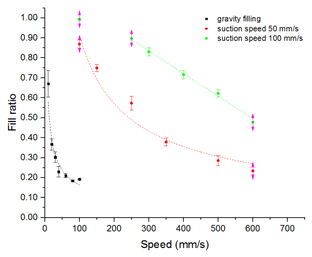

Lactose monohydrate

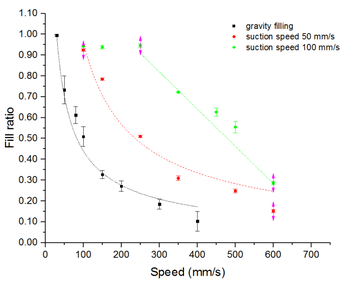

MCC PH102

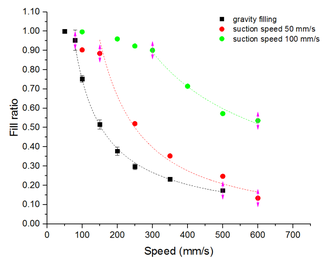

MCC CP102

The efficiency of die filling increases significantly with suction filling. This increase is particularly evident for more cohesive Lactose and MCC PH102, although the filling efficiency of such free flowing and coarse product as CP102 are also improved by the suction.

Influence of powder properties on die filling efficiency

The correlation of the critical filling velocities [1] of different powders with such powder properties as average particle size (d50), specific energy, pressure drop, cohesion and flow function were explored.

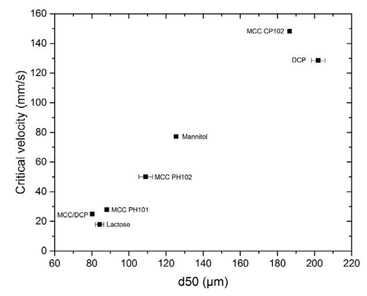

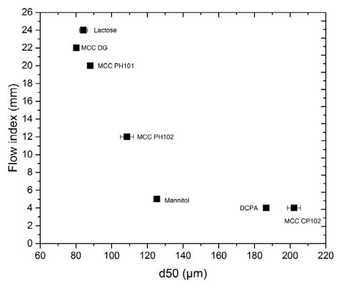

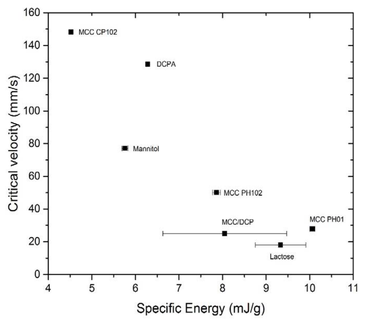

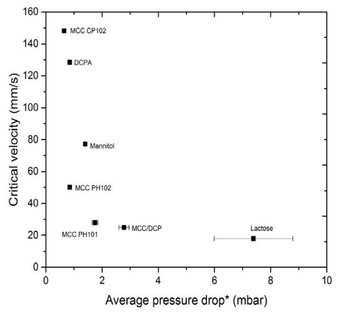

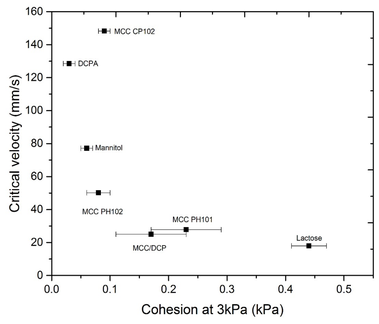

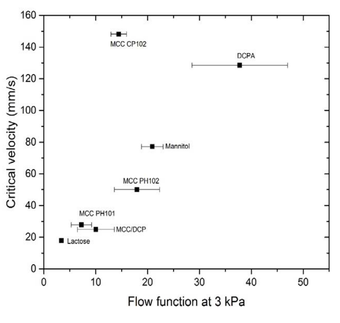

5. Conclusions

1. For gravity filling, the rotary system performs better than the linear system. But at higher speeds, the effect of cohesion prevails.
2. The suction filling improves significantly the fill ratio: especially for cohesive powders with smaller particle size, as has been observed by Mills et al [2].
3. Higher critical fill velocity are associated with larger particle size and higher flow function value, lower specific energy, average pressure drop and cohesion.

5. Future work

- ❑ Evaluation of the impact of powders properties on the efficiency of suction die filling.
- ❑ Study of multicomponent blends, with the focus on uniformity of model API distribution within the die and the influence of process parameters (fill and suction speed) on the content uniformity.
- ❑ Investigation of forced die filling, for which a paddle powder feeder will be designed and fitted into the die filling apparatus. The die filling efficiency will then be explored.

Reference

[1] Wu, C. Y., Dihoru, L., & Cocks, A. C. F. (2003). The flow of powder into simple and stepped dies. *Powder Technology*, *134*(1–2), 24–39.

[2] Mills, L. A., & Sinka, I. C. (2013). Effect of particle size and density on the die fill of powders. *European Journal of Pharmaceutics and Biopharmaceutics*, *84*(3), 642–652.

[3] Freeman, R., & Fu, X. (2008). Characterisation of powder bulk, dynamic flow and shear properties in relation to die filling. Powder Metallurgy, 51(3), 196–201.

MULTI-SCALE MODELING OF COMPACTION WITH EMPHASIS ON POWDER MIXTURES

Antonios Zavaliangos
Department of Materials Science and Engineering, Drexel University, Philadelphia, PA19104, USA

OBJECTIVES

- Understanding the rules that determine the compaction and properties of multicomponent formulations

APPROACH

- Develop a discrete element framework for the analysis of compaction and mechanical properties of multicomponent mixtures
- Identify geometric and material parameters that control the behavior of such mixtures
- Validate the analysis

DEM: Force displacement law for High Density Extraction of material parameters from data

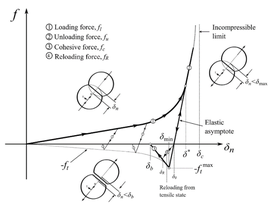

INCLUDES COHESION → STRENGTH

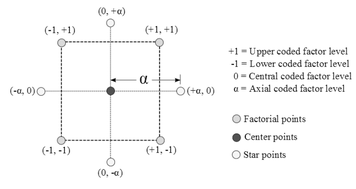

Initial methodology

Experimentally: Same as for FEM models (e.g., DPC)
Numerically: 34 DEM runs to create the response surface and a quick optimization. To be repeated for every new material. Old results not used

New methodology

Numerically: Bayesian approximation, a popular methodology in machine learning, decision making. Calibration of new materials is requires a reduced number of runs.
Old results guide the new calibration

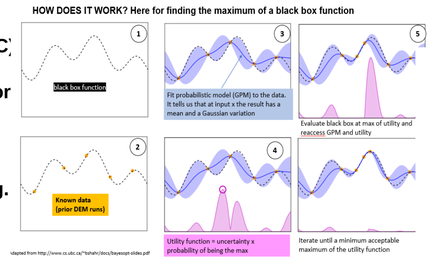

1) **Small deformation regime** - contacts are independent from others
2) **Contact interaction regime** – each contact "feels" the presence of its neighbors
3) **Low compressibility regime** – where the porosity closing locally and elasticity dominates

Predictions

From last year:
DEM offers a much better prediction of residual radial wall stress in compaction than FEM
DEM predicts the connection between interparticle strength and radial wall stress and post compaction expansion

This year:
Explored the effect of initial packing on strength.
Two RD0=0.23 and 0.31 (via vibration)

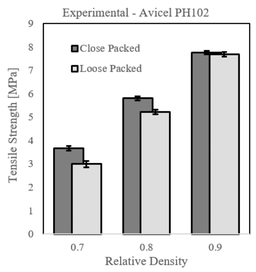

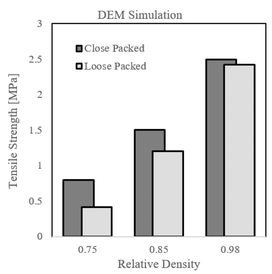

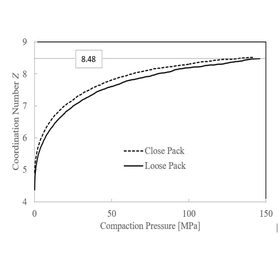

Residual stress: an important factor in strength of mixtures

A+B mixture
A=B except in elastic modulus

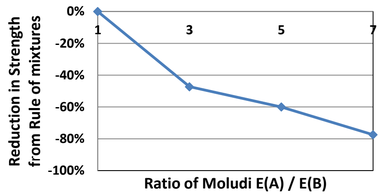

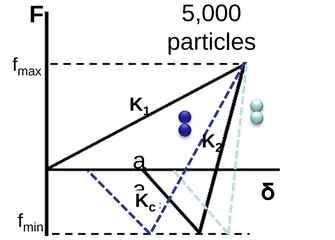

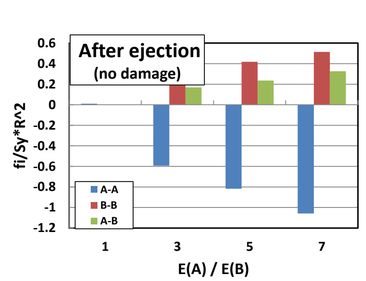

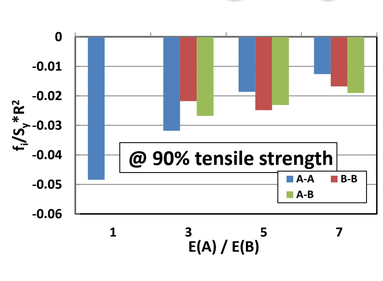

Understanding the strength of compacts

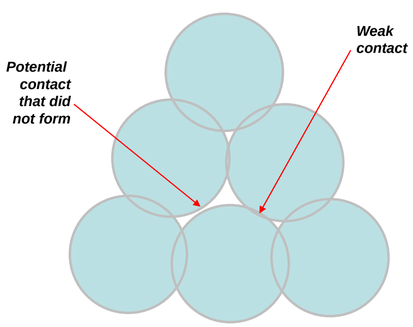

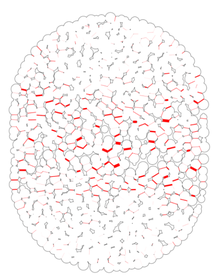

$$D_2 = 1 - \frac{\sum(\min(\delta, \delta_{min}) - \delta_b)}{\sum(\delta_{min} - \delta_b)}$$

Additional predictions

Improved strength in triaxial unloading in line with Hiestand experiments

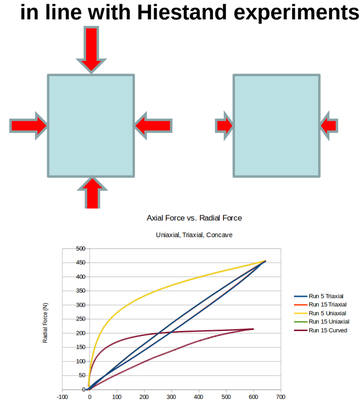

Fundamental highlights of the sticking phenomenon

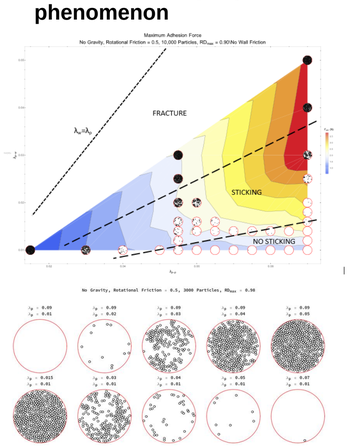

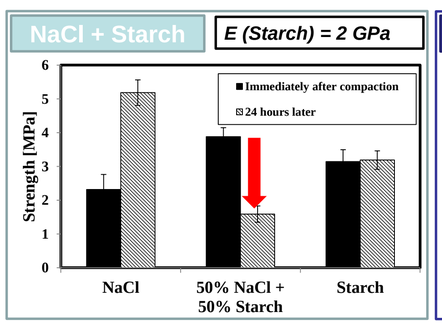

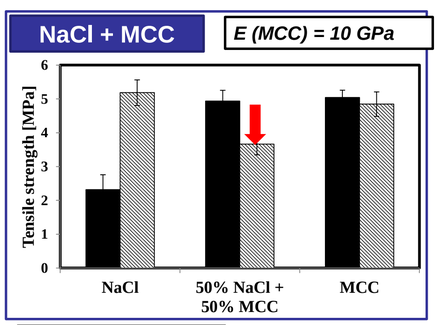

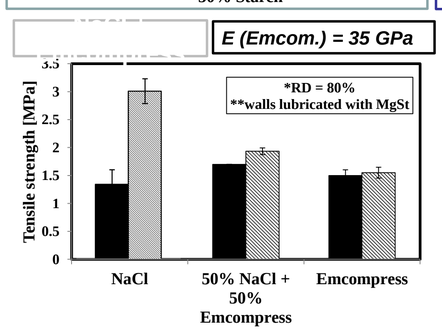

- Testing the DEM supported hypothesis that smaller difference in elastic moduli between NaCl and the second phase would result in smaller residual stress leading to less or no reduction in strength of a mixture

IFPRI
International Fine Particle Research Institute